

# SOD1 Exhibits Allosteric Frustration to Facilitate Metal Binding Affinity

Atanu Das\* and Steven S. Plotkin\*

\*Department of Physics and Astronomy, University of British Columbia, Vancouver, Canada

Superoxide dismutase-1 (SOD1) is a ubiquitous, Cu and Zn binding, free radical defense enzyme whose misfolding and aggregation play a potential key role in amyotrophic lateral sclerosis, an invariably fatal neurodegenerative disease. Over 150 mutations in SOD1 have been identified with a familial form of the disease, but it is presently not clear what unifying features, if any, these mutants share to make them pathogenic. Here, we develop several new computational assays for probing the thermo-mechanical properties of both ALS-associated and rationally-designed SOD1 variants. Allosteric interaction free energies between residues and metals are calculated, and a series of atomic force microscopy experiments are simulated with variable tether positions, to quantify mechanical rigidity “fingerprints” for SOD1 variants. Mechanical fingerprinting studies of a series of C-terminally truncated mutants, along with an analysis of equilibrium dynamic fluctuations while varying native constraints, potential energy change upon mutation, frustratometer analysis, and analysis of the coupling between local frustration and metal binding interactions for a glycine scan of 90 residues together reveal that the apo protein is internally frustrated, that these internal stresses are partially relieved by mutation but at the expense of metal-binding affinity, and that the frustration of a residue is directly related to its role in binding metals. This evidence points to apo SOD1 as a strained intermediate with “self-allostery” for high metal-binding affinity. Thus, the prerequisites for the function of SOD1 as an antioxidant compete with apo state thermo-mechanical stability, increasing the susceptibility of the protein to misfold in the apo state.

allostery and cooperativity | mechanical stability | protein misfolding | frustration | ALS

Abbreviations: (F,S)ALS, (familial, sporadic) amyotrophic lateral sclerosis; WT, wild-type; ZBL, Zn-binding loop; ESL, electrostatic loop; RMSF, root mean squared fluctuations; SASA, solvent-accessible surface area; PTM, post-translational modification; Cu,Zn(SS), holo, disulfide present; E,E(SH), apo, disulfide-reduced; WHAM, weighted histogram analysis method; SI, Supporting Information Appendix

**A**llosteric regulation canonically involves the modulation of a protein’s affinity for a given ligand A through the binding of a separate ligand B to a distinct spatial location on the protein. The modulatory binding site at the distinct location is referred to as the allosteric site, and the interaction between the allosteric site and the putative agonist binding site is referred to as an allosteric interaction. Early models of allostery were used to explain ligand saturation curves for hemoglobin in terms of subunit interactions that would induce binding cooperativity [1,2]. Cooperativity may be quantified through the non-additivity in the binding energies of ligand and allosteric effector [3]. More recently, allostery has been thought to be a more generic property present even in single domain proteins [4]. In this context, positive cooperativity may be modulated through frustrated intermediates [5], which may enhance the conformational changes observed upon ligand binding for allosteric proteins [6]. In a single domain protein, the notion of an allosteric effector can be generalized

to intrinsic protein side chains that can enhance protein function or functionally important motion at the expense of native stability- a kind of “self-allostery”. Some allosteric activation mechanisms involve mediation of conformational switches by non-native intra-protein interactions [7], an effect predicted by energy landscape approaches wherein barriers between conformational states are buffed to lower energies [8]. The potential for novel allosteric regulators may vastly broaden candidate targets for drug discovery [9]. The internal frustration required for cooperative allosteric function may have deleterious consequences however, if protein stability is sufficiently penalized in intermediate states to enhance the propensity for misfolding and subsequent aberrant oligomerization, processes known to be involved in neurodegenerative disease [10]. Here we show that the ALS-associated protein Cu, Zn superoxide dismutase (SOD1) is embroiled in such a conflict between stability and function.

SOD1 is a homo-dimeric antioxidant enzyme of 32kDa, wherein each monomer contains 153 amino acids, binds one Cu and one Zn ion, and consists largely of an eight stranded greek key  $\beta$  barrel with two large, functionally important loops [11,12,13]. Loop VII or the electrostatic loop (ESL, residues 121-142) enhances the enzymatic activity of the protein by inducing an electrostatic funnel towards a redox active site centered on the Cu ion [14]. Loop IV or the Zn-binding loop (ZBL residues 49-83), contains histidines H63, H71, and H80 as well as D83, which coordinate the Zn ion and, along with a disulfide bond between C57 and C146, enforce concomitant tertiary structure in the protein. The Cu on the other hand is coordinated by H46, H48, and H120, and the bridging histidine H63 between the Cu and Zn, which are located primarily in the Ig-like core of the protein.

SALS inclusions are immunoreactive to misfolding-specific SOD1 antibodies [15,16]. Such misfolded aggregates may be initiated from locally (rather than globally) unfolded states that become accessible, for example, via thermal fluctuations or rare events [17], e.g. near-native aggregates or aggregation precursors were found for an obligate monomeric SOD1 variant [18], and for FALS mutants S134N [19,20] and E,E(SS) H46R [19]. These above studies have motivated the present computational study, which focuses on the native and near-native thermo-mechanical properties of mutant, WT and post-translationally modified SOD1.

## Results

**Cumulative distributions of work values can discriminate SOD1 mutants and premature variants.** Mechanical probes were employed by simulating tethers on the residue closest to the center of mass of the SOD1 variant, and on various residues on the protein surface. The experimental analogue

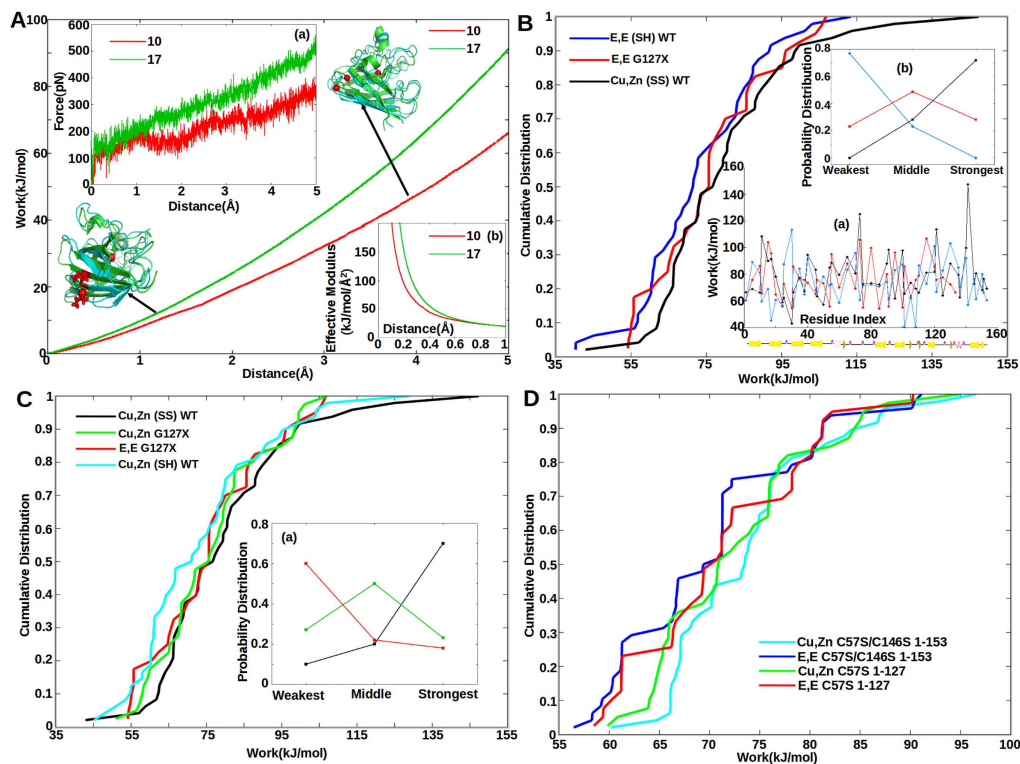


**Fig. 1.** (Panel A) Force (inset a), Work (main panel), and effective modulus (inset b) as a function of extension. Tethers are placed at the  $C_{\alpha}$  atom closest to the center of mass of the SOD1 monomer (H46), and the  $C_{\alpha}$  atom of either residues G10 (red) or I17 (green), in separate pulling assays. Ribbon representations of the protein are also shown; the tethering residue is shown in licorice rendering (in red) and the center  $C_{\alpha}$  as a red sphere. The initial equilibrated (at 0 Å, green ribbon) and final (at 5 Å, blue ribbon) structures are aligned to each other by minimizing RMSD. (Panel B) (Inset a) Work profiles of Cu,Zn(SS) WT (black), E,E(SH) WT (blue), and E,E G127X SOD1 (red) vs. sequence index. Secondary structure schematic is shown underneath. (Main panel) Cumulative distributions of the work values in inset (a). E,E G127X is more stable than full-length E,E (SH) SOD1 ( $p=9e-7$ ). (Inset b) Fraction of the 48 incidences that each variant had either the weakest, strongest, or middle work value, e.g. E,E(SH) SOD1 is weakest 80% of the time and is never the strongest variant. (Panel C) Cumulative work distributions for Cu,Zn (SS) WT (black), Cu,Zn G127X (green), E,E G127X (red), and Cu,Zn (SH) WT (cyan). Cu,Zn G127X is destabilized with respect to full-length Cu,Zn (SS) WT ( $p=6.2e-8$ ). (Inset a) Same analysis as panel B, inset b, for the variants Cu,Zn(SS) WT, Cu,Zn G127X, and E,E G127X. (Panel D) Cumulative distributions for serine mutant SOD1 variants demonstrate that C-terminal truncation stabilizes the apo form but destabilizes the holo form (see text).

to such an *in silico* approach would require multiple AFM or optical trap assays involving numerous residue pairs about the protein surface as tethering points. This is difficult and time-consuming to achieve in practice, which thus provides an opportunity for the present simulation approaches. All proteins in this study were taken in the monomeric form—many of them such as E,E(SH) SOD1, G127X, and G85R are either naturally monomeric or have significantly reduced dimer stability. The ALS-associated truncation mutant G127X contains a frameshift insertion which results in 6 non-native amino acids following Gly127, after which a truncation sequence terminates the protein 20 residues short of the putative C-terminus [21,22]. Here PTMs refer to processes involved in the *in vivo* maturation of SOD1, including disulfide bond formation, and metallation by Cu and Zn.

The simulated force-extension profile may be used to obtain the work required to pull a given residue to a given distance (Fig. 1A). In this assay, we found that large effective

stiffness moduli were observed for small perturbing distances (Fig. 1A inset b). These were attributable primarily to side chain-side chain “docking” interactions in the native structure (SI Appendix, Fig. S2). The work to pull a given residue to a distance sufficient to constitute an anomalously large fluctuation, e.g. 5 Å, can be calculated as a function of sequence index for a given SOD1 variant, resulting in a characteristic mechanical profile or “mechanical fingerprint” for that protein (Fig. 1B, inset a). The work values at 5 Å do not correlate with RMSF values of the corresponding residues [23]. A representative subset of 48 residues was obtained as described in the SI. We found that such a profile was independent of how the protein was initially constructed before equilibration, i.e. from what PDB, but was clearly different between WT SOD1 and mutants such as G127X, as well as other PTM variants such as E,E(SH) SOD1 (SI Fig. S4). Table S1 in SI gives the correlation coefficients between variants. A given PTM globally modulates the mechanical profile, inducing both local and non-local changes in stability that can be both destabilizing

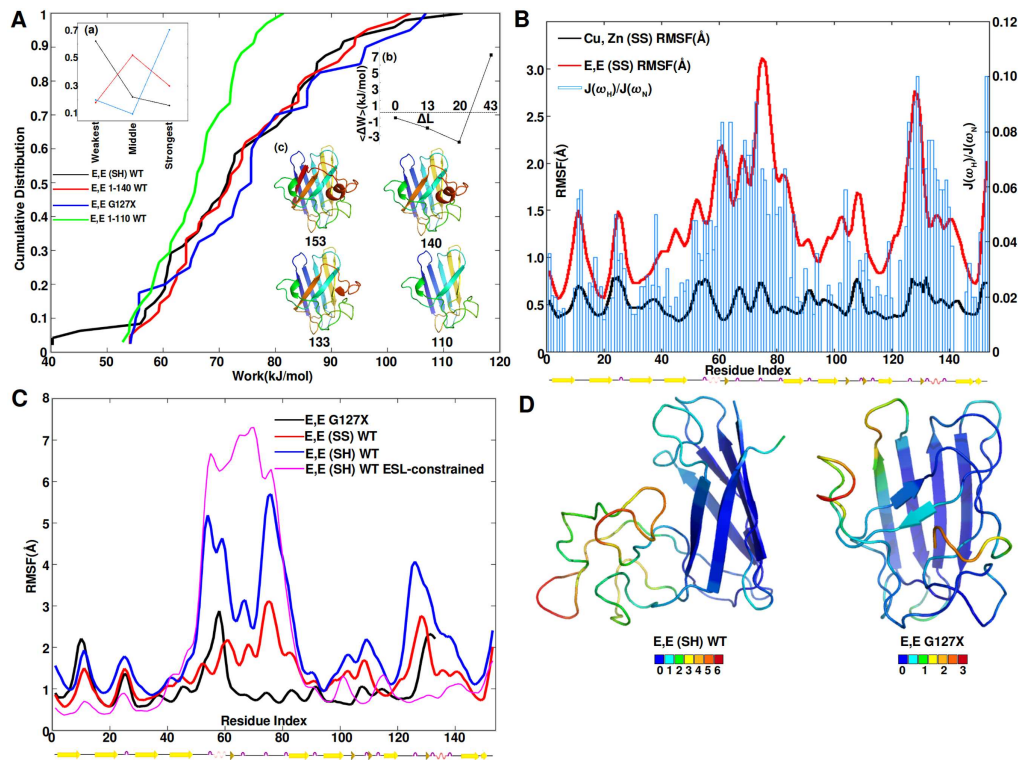


**Fig. 2.** (Panel A) Cumulative distributions of work values for C-terminal-truncated SOD1 variants of variable sequence length show a non-monotonic trend in mechanical stability. All variants are metal-depleted and have no disulfide bond. Sequences are given in the legend (see text). (Inset a) Comparing the cumulative distributions in the main panel, that of the mutant G127X is most commonly the strongest, full-length SOD1 is most commonly the weakest, and 1-140 is most often in the middle. (Inset b) Change in work value  $\overline{W}_{MUT} - \overline{W}_{WT}$  averaged over residues, as a function truncation length, for the SOD1 variants in the main panel. (Inset c) Ribbon schematics of the various truncation mutants, colored blue to red from N- to C-terminus, labeled by C-terminal residue. (Panel B) Simulated native-basin dynamical fluctuations (RMSF) in explicit SPC solvent, for Cu,Zn(SS) (black) and E,E(SS) SOD1 monomer (red), along with the experimentally measured ratio of spectral density functions  $J(\omega_H)/J(\omega_N)$  of obligate monomeric E,E(SS) F50E/G51E/E133Q SOD1 (blue bars) [31]. Correlation coefficient is  $r = 0.78$ . (Panel C) Simulated RMSF for SOD1 variants E,E G127X (black), E,E(SS) (red), E,E(SH) (blue), and E,E(SH) with the ESL constrained to be natively structured (magenta). The presence of native stress is indicated by the increased disorder of the ZBL upon structuring the ESL (see text). (Panel D) Snapshots of typical structures of E,E(SH) and G127X SOD1 from equilibrium simulations, color coded by the mean RMSF for each residue; RMSF increases from blue to red according to the scale bars shown.

in some regions and stabilizing in others. A detailed study of the mechanical consequences of mutations or PTMs, e.g. by studying the long-range communication through interaction networks in the mutant vs WT protein (see e.g. [24,25,26,27]) is an interesting topic of future research.

We also found that the mechanical work profile was nearly independent of whether an explicit or implicit solvent model was used in the simulations, even though native basin fluctuations (RMSF) showed significant scatter in comparing implicit and explicit solvent models (SI Fig. S5). Equilibrium fluctuations are much more sensitive to solvent models than the large scale perturbations we consider here. On the other hand, a structure-based Gō model does only a modest job of capturing the mechanical profile, and is poor in particular for residues where electrostatic interactions play a significant role in stability (SI Fig. S6). Interestingly, the default energy scale of 1 kJ/mol for each contact or dihedral interaction used in current

Gō models [28] captures the overall energy scale of the work profile quite well for SOD1, though it must likely be modified for other proteins such as thermophilic proteins.

In support of the thermodynamic relevance of a SOD1 variant's mechanical fingerprint, we found that the non-equilibrium work values obtained by pulling a residue to 5Å strongly correlate with the equilibrium free energy change for the same process, as calculated using the WHAM method ( $r=0.96$ , SI Fig. S7). Thus, the work profiles obtained are an accurate measure of the corresponding local thermodynamic stability profile, up to a scaling factor.

Comparing the mechanical fingerprints of E,E(SH) SOD1 and that of G127X (Fig. 1B, inset a), we see that many discrepancies between SOD1 variants and WT are difficult to disentangle solely from the work profile, or even from histograms of the work values (SI Fig. S3). However, the mechanical discrepancies emerged quite naturally from the cumulative distribution of work values. Mechanical scans were thus used to construct the cumulative distributions, which then al-

lowed us to distinguish stabilizing energetics in various forms of PTM SOD1, e.g. between E,E(SH), G127X, and Cu,Zn(SS) SOD1 in Figure 1B. Not all residues needed to be sampled to obtain the cumulative distribution- we found convergence to within  $\approx 1$  kJ/mol after a sample size of about 40 residues (SI Fig. S8). This does not mean the mechanical profile obtained from 48 residues is representative of the stability in the corresponding regions of the protein: the mechanical work values were essentially uncorrelated for amino acids about 3 residues apart.

Comparison of the cumulative work distributions shows that the ALS-associated mutant Cu,Zn(SS) A4V is slightly more mechanically malleable than Cu,Zn(SS) WT, particularly in the weaker regions of the protein (SI Fig. S13). However the mechanical weakening due to mutation is substantially larger in the E,E(SS) state, and largest in the E,E(SH) state (green curves in SI Fig. S13). Experimental measurements of melting temperature also have shown increased susceptibility to mutation in the E,E(SH) state for A4V [29]. We also note from SI Figure S13 that disulfide reduction in the WT apo state, E,E(SS) $\rightarrow$ E,E(SH), actually increases the rigidity of the native basin [23], even though the net thermodynamic stability is decreased, primarily due to increased unfolded entropy [30].

**Lack of post-translational modifications mechanically destabilizes SOD1, however the truncation mutant G127X stabilizes the apo, disulfide-reduced protein..** The cumulative distribution of E,E(SH) lies to the left of that for Cu,Zn(SS) SOD1 in Figure 1B for all rank-ordered work values, illustrating that that variant is more malleable and thus more susceptible to perturbing forces that might induce the conformational changes accompanying misfolding. Likewise, Cu,Zn(SH) is destabilized with respect to Cu,Zn(SS) in Figure 1C, and the other PTM variants in SI Figure S14 show that lack of PTMs reduces the mechanical rigidity.

On the other hand, the E,E G127X truncation mutant, which lacks both metals, a disulfide bond, and part of the sequence, shows *increased* mechanical stability over E,E(SH) WT ( $p = 9e-7$ , Fig. 1B). Comparing the profiles, E,E(SH) is most commonly the weakest, Cu,Zn(SS) is most commonly the strongest, and G127X is most commonly in the middle (Fig. 1B Inset b). Apparently the C-terminal region of the protein mechanically stresses the remainder of the protein *when PTMs are absent*, reducing its mechanical stability. However, a metastable holo variant of G127X containing metals in their putative positions is *less* mechanically stable than holo WT ( $p = 6.2e-8$ , Fig. 1C). In the full-length holo protein, native stabilizing interactions are more apt to be minimally frustrated, and thus C-terminal truncation induces softening of the native structure. The metallation of G127X only marginally stabilizes it ( $p = 6.7e-3$ , Fig. 1C inset a), while metallation of WT protein results in substantial mechanical stabilization (SI Fig. S14). G127X lacks C146, so Cu,Zn(SH) WT may be a more appropriate comparison than Cu,Zn(SS) WT. Cu,Zn(SH) SOD1 is less stable than either Cu,Zn G127X or E,E G127X (Fig. 1C), however Cu,Zn(SH) contains a protonated Cysteine C146, which is destabilizing, and not present in G127X.

To deconvolute the effects of protonated Cysteines, we examined a set of 4 serine mutant proteins: Cu,Zn C57S/C146S 1-153 (full length), E,E C57S/C146S 1-153, Cu,Zn C57S 1-127 (truncated at residue 127), and E,E C57S 1-127. For this system of proteins, Cu,Zn C57S/C146S 1-153 is clearly the most stable over most of the range of work values (Fig. 1D), and Cu,Zn C57S 1-127 is destabilized with respect to it. E,E

C57S 1-127 is further destabilized with respect to its holo form, but is *more* stable than the full length apo form E,E C57S/C146S 1-153. This demonstrates that C-terminal truncation stabilizes the apo form but destabilizes the holo form. This conclusion is robust to changes in pulling distance (SI Fig. S15).

**Short length C-terminal truncation mechanically stabilizes the apo protein, while sufficiently long C-terminal truncation destabilizes it..**

The mechanical properties of two additional truncated constructs, E,E 1-140 (WT sequence), and E,E 1-110, were assayed to investigate the crossover from increased to eventually reduced mechanical stability as the length of truncation is increased (Fig. 2A inset b). All truncation variants are missing the putative disulfide bond. Figure 2A shows cumulative distributions for the above variants along with E,E(SH) SOD and E,E G127X. The truncation E,E 1-140 mechanically stabilizes E,E(SH) SOD1 ( $p = 1e-3$ ), and G127X is further stabilized with respect to 1-140 ( $p = 9e-4$ ). Comparison of the triplets of rank-ordered work values corresponding to E,E(SH), E,E 1-140, and E,E G127X supports this conclusion (Fig. 2A inset a). We have omitted the 3 least stable work values for all variants in calculating statistical significance- these are outliers for E,E(SH) that would dominate the result towards the conclusion that we have arrived at without their inclusion. Variant E,E 1-110 has significantly compromised mechanical rigidity and may not be thermodynamically stable- the mechanical assay only probes malleability of the native basin.

**Simulated fluctuations correlate with experimental spectral density functions for apo SOD1..**

We performed 20ns equilibrium simulations in explicit solvent (SPC water model) for Cu,Zn(SS) and E,E(SS) SOD1. Native-basin RMSF values show significant scatter between explicit and implicit solvent models compared to mechanical work values (SI Fig. S5), so for analysis of equilibrium fluctuations, explicit solvent is used. Figure 2B plots the resulting equilibrium RMSF for Cu,Zn(SS) and E,E(SS) SOD1; SI Figure S9 also gives the solvent-accessible surface area of backbone amide Nitrogens ( $SASA_N$ ) for the same equilibrium trajectory. The main effect of metal loss is to induce solvent exposed, disordered, and dynamic Zn-binding and electrostatic loops (loops IV and VII). A moderate increase in dynamics is observed for loop VI as well. The preferential increase in dynamics of the ZBL and ESL upon metal loss is consistent with experimental measurements of the ratio of spectral density functions  $J(\omega_H)/J(\omega_N)$ - a measure of dynamics fast compared to the tumbling rate (correlation coefficient  $r = 0.78$ ). The experimental measurements of spectral density [31] are obtained for a monomeric E,E(SS) SOD1 mutant F50E/G51E/E133Q [32].

**Dynamic fluctuations in C-terminal truncation mutants reveal native frustration in apo SOD..**

Because G127X is more mechanically stable than E,E(SH) SOD1, native basin fluctuations were investigated to see if the extra stability of G127X was recapitulated in equilibrium dynamics. Figure 2C shows that indeed the RMSF are substantially enhanced in E,E(SH) relative to G127X, in particular in the ZBL and ESL (loops IV and VII). This is true even though  $\beta$ -strand 8, N-terminal to the ESL, constrains E,E(SH) and is absent in G127X. Though more dynamic and mechanically malleable, E,E(SH) is not more solvent-exposed (by  $SASA_N$ ) than G127X, indicating a collapsed, dynamic globule with non-native interactions (SI Fig. S10). As well, E,E(SH) is more dynamic than E,E(SS) SOD1 (Fig. 2C), but less solvent exposed than E,E(SS), particularly in the ZBL and ESL (SI Fig. S10). Collapse and non-

native interactions are not hindering the dynamics of the ZBL and ESL; snapshots from simulations for E,E(SH) WT and G127X are shown in Figure 2D. Similar condensation phenomena are also observed in prion protein [33] and NHERF1 [34]. In a large scale study of 253 proteins across several fold families [35], RMSF and SASA showed poor correlation ( $r \approx 0.35$  for backbone carbons).

It is intriguing that the additional constraint of structuring  $\beta 8$  in E,E(SH) SOD1 results in enhanced rather than suppressed disorder in the ZBL. One potential explanation is that because there is more residues in the ESL present in E,E(SH) than in G127X, the ESL forces the ZBL to be more expanded by steric repulsion, and thus more dynamic, i.e. a “polymer brush” effect. Another possible explanation is that the order induced by structuring  $\beta 8$  in E,E(SH) SOD1 induces frustration and consequent strain elsewhere in the protein, resulting in induced disorder in the ZBL. We differentiated these two scenarios by applying native constraints between the  $C_\alpha$  atoms in the ESL and the rest of protein, but excluding contacts between the ESL and the ZBL: harmonic springs were applied to all pairs of  $C_\alpha$  atoms within 4Å in the native holo structure that involved contacts either within residues 133-153, or between residues 133-153 and either residues 1-40 or 90-153. This procedure further constrains the ESL and  $\beta 8$  to be natively structured, removing any polymer brush effect, but enhancing any native strain. Consistent with a model involving native frustration, the ZBL loop IV becomes *more* disordered in E,E(SH) SOD1 upon implementing ESL/ $\beta 8$  native constraints (Fig. 2C).

**“Frustratometer” results and potential energy changes support increased frustration in apo WT SOD1 with respect to apo ALS-associated mutants.** Typically frustrated contacts, according to the “frustratometer” method developed by Wolynes and colleagues [5], were found by averaging 50 snapshots from an equilibrium ensemble for WT SOD1, and for each of 22 ALS-associated SOD1 mutants (SI Table S3). Both E,E(SS), and Cu,Zn(SS) states were analyzed. Results were averaged over the 22 mutants to yield the mean number of frustrated contacts at a given residue position, for the “average” mutant. Taking the difference of this quantity with that for WT SOD1 gives the mean change in frustration upon mutation, which increased for holo SOD1 by about 5 total contacts, but *decreased* for apo SOD1 by about 22 total contacts (Fig. 3A). This result again supports a frustrated apo state in SOD1. Direct computation shows on average about 38 more highly-frustrated contacts in E,E(SS) SOD1 than in Cu,Zn(SS) SOD1 (SI Fig. S17).

For the same set of mutants, we found that the ensemble-averaged total potential energy in the native state increased upon mutation for the Cu,Zn(SS) protein, but decreased upon mutation in the E,E(SS) protein. This is consistent with the above frustratometer results. The “time-resolved” change in potential energy  $\Delta U$  upon *in silico* mutation for a representative mutant (G37R) is shown in Figure 4A. The distribution of potential energy changes for the 22 ALS-associated mutants listed in SI Table S3 is shown in Figure 4B, which shows potential energy “cost” upon mutation for Cu,Zn(SS) mutants, but a significant shift towards negative stabilizing values for E,E(SS) mutants. The same conclusion is obtained from 30 non-ALS alanine mutants (SI Fig. S18). Figure 4C shows that the net effect of mutation on the potential energy is to increase it on average in the holo state, but to *decrease* it on average in the apo state, indicating stabilization. Moreover, all ALS mutants facilitate metal release [23]; the net effect of mutation on the Cu and Zn binding free energies is to decrease

both of them. Thus mutations relieve stress in the apo state, while inducing loss of metal binding function. It thus appears that apo SOD1 has evolved to have high affinity for metals at the expense of native stability and increased frustration.

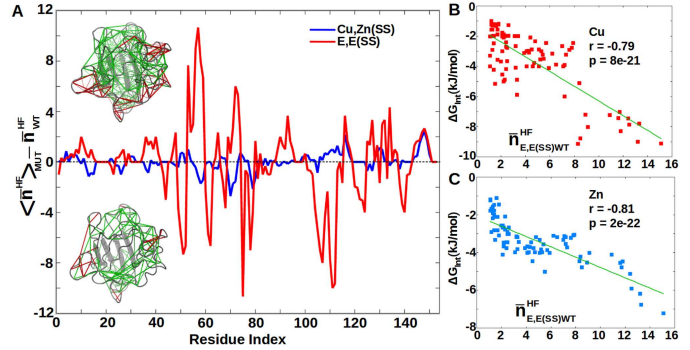


**Fig. 3.** (A) Frustrated contacts (in red) and unfrustrated contacts (in green) for E,E(SS) WT SOD1. (B) Same contacts as (A) for the average over 22 ALS E,E(SS) mutants (see text). (C) The mean number of frustrated contacts within a sphere of radius 5Å centered on each  $C_\alpha$  atom, is found as a function of residue index. Ensemble averages are taken from 50 snapshots in an equilibrium simulation. This is done for both the Cu,Zn(SS) state and the E,E(SS) state, for both the WT sequence, and for 22 mutant sequences. The 22 mutant sequences are averaged to obtain the ensemble and mutant averaged number of contacts as a function of residue index  $i$ ,  $\langle n^{HF}(i) \rangle_{MUT}$ . Plotted is the difference between  $\langle n^{HF}(i) \rangle_{MUT}$  and the corresponding numbers for the WT sequence  $\bar{n}_{E,E(SS)WT}^{HF}(i)$ . A positive number would indicate an increase in frustration upon mutation. Holo state is shown in blue and has an average of +5 contacts; apo state is shown in red and has an average of -22 contacts. (B) Interaction free energy between a residue’s side chain and the Cu ion, plotted as a function of the E,E(SS) ensemble-averaged number of highly-frustrated contacts that residue has ( $r = -0.79$ ,  $p = 8e-21$ ). (C) Same as in Panel B but for the Zn ion ( $r = -0.81$ ,  $p = 2e-22$ ).

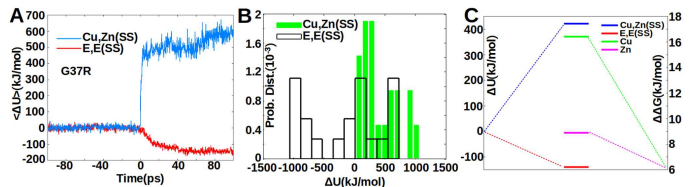


**Fig. 4.** (A) Change in potential energy  $\Delta U(t)$  as a function of *in silico* time, before and after implementing the mutation G37R. (B) Distribution of the asymptotic potential energy change  $\Delta U(\infty)$  for 22 ALS mutants (see text). (C) Mean potential energy change averaged over mutants, for both the holo state and the apo state, along with the mean difference, WT minus mutants, in both Cu and Zn binding free energy.

**Frustrating residues in the apo state are allosteric effectors, and positively modulate metal affinity in proportion to their frustration.** To test the extent to which the residues facilitating metal binding are frustrated, we have calculated the interaction free energy of each WT residue with both Cu and Zn, by considering thermodynamic cycles [3] involving metallation and residue “insertion” from a glycine at the corresponding position (e.g. G4A). The interaction free energy  $G_{int}$  between each residue side-chain and either Zn or Cu is given (here specifically for residue Ala 4 with Zn) by

$$\begin{aligned} G_{int} &= \Delta G(G \rightarrow A, O \rightarrow Zn) - \Delta G(G \rightarrow A, O) - \Delta G(G, O \rightarrow Zn) \\ &= \Delta G(A, O \rightarrow Zn) - \Delta G(G, O \rightarrow Zn) \end{aligned} \quad [1]$$

where  $\Delta G(A, O \rightarrow Zn)$  is the free energy change of Zn insertion when alanine is present at position 4, and  $\Delta G(G, O \rightarrow Zn)$  is

the free energy change of Zn insertion when glycine (no side chain) is present at position 4. The other residues, and Cu interactions, are handled analogously (see SI Methods).

Figures 3B,C plot the above interaction free energy of a residue with Cu or Zn, *vs.* the E,E(SS) ensemble-averaged number of highly-frustrated contacts that residue has. Data are obtained for 90 glycine mutants listed in SI Table S3, for residues that had at least one highly-frustrated contact (see SI). The values of  $G_{int}$  for all 90 mutants listed in SI Table S3 are negative, indicating cooperative interactions, wherein the WT residue facilitates binding of the metal. Each of these residues can be thought of as allosteric effectors, positively modulating affinity for either metal. For both Cu and Zn, the larger the degree of frustration in the apo state, the larger the role that residue has in facilitating metal binding. No such trend is seen for Cu,Zn(SS) SOD1 (SI Fig. S18). This result strongly supports a model of the apo state as an allosteric intermediate designed for high metal binding affinity at the expense of structural stability.

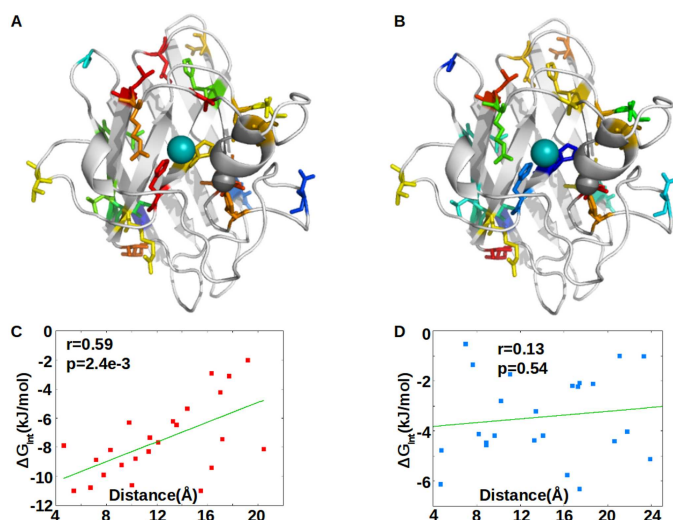


**Fig. 5.** Panel (A): Residues color-coded by interaction energy with the Cu ion (depicted as a cyan sphere). The extent of interaction is strongest in magnitude for red colored residues and decreases to blue. Panel (B): same as (A) for the Zn ion (depicted as a grey sphere). Panel (C): Interaction energy with Cu correlates with the distance of the residue from the Cu ion; residues in close proximity more strongly interact. Panel (D): Interaction energy with Zn does not correlate with distance of the residue to the Zn ion, indicating non-local allosteric effects.

Finally, we test the distance-dependence of the interaction free energy with the metals, for the set of 24 ALS-associated mutants in SI Table S3. In the case of Cu, the allosteric regulation for metal affinity is significantly correlated with the proximity of the residue to the Cu binding site (Fig. 5A,C). Interestingly, the allosteric regulation for Zn binding is uncorrelated with distance to the Zn binding site and thus non-local. This finding is consistent with experimental results that Zn binding is concomitant with large structural change (partial folding) of the protein [36]. Long-range coupling to the Zn-binding region has also been observed in G93A SOD1 [37]. The same conclusion is obtained for the 90 frustrated residues given in SI Table S3 (SI Fig. S19).

## Discussion

We have found here a connection between the allosteric design of residues in premature superoxide dismutase towards high metal-binding affinity, and the consequent frustration in the apo state of the protein. A variety of results supported this conclusion. Mechanical profiles were obtained from *in silico* AFM assays with variable tether positions; in this context it was found that the C-terminal truncation mutant G127X had higher mechanical rigidity than E,E(SH) SOD1, implying the release of internal stresses upon removal of part of the protein. Large truncation lengths eventually destabilized the protein.

The higher malleability of E,E(SH) SOD1 over G127X is recapitulated by larger equilibrium dynamical fluctuations in the native basin. Constraining loop VII (the ESL) to be natively structured only increases fluctuations in loop IV (the ZBL), ruling out polymer brush effects and supporting the native stress hypothesis.

Implementing Wolynes’s “frustratometer” method [5] shows that, perhaps surprisingly, more frustration is present on average in the WT apo state than is present for apo mutants. For the holo state the situation is reversed however, which is consistent with the notion that mutants facilitate metal release. In fact every ALS-associated mutant we have studied lowered the affinity for both Cu and Zn [23]. We have found here that while these mutants raise the potential energy of the holo state, they tend to lower the potential energy of the apo state and thus stabilize it, consistent with frustratometer results. A general comparative analysis of the decrease in potential energy and frustration for apo ALS-associated mutants, along with the results from their individual mechanical scans which generally show weakening with respect to local perturbations, is an interesting topic for future work. SI Figure S20 compares the relevant quantities for the ALS mutants A4V and G127X.

Residues in apo SOD1 can be thought of as allosteric effectors for metal binding. By considering the cooperativity in thermodynamic cycles involving mutation to glycine and metal release, we quantified the interaction free energies between residues in the protein and either Cu or Zn. All interaction energies were negative, indicating positive modulation of metal affinity. Moreover we found that function frustrates stability: the stronger the interaction energy, the more frustrated the residue. For Cu, the strength of the interaction significantly correlates with proximity to the binding site. For Zn however, there is no correlation with proximity, indicating a non-local allosteric mechanism involving propagation of stress-release throughout the protein, and consistent with the large structural changes accompanying Zn binding.

The above evidence points towards a paradigm wherein sequence evolution towards high metal affinity results in a trade-off for significant native frustration in the apo state of SOD1. A similar conclusion has been reached from studies of a SOD1 variant with Zn-coordinating ligands H63, H71, H80, and D83 mutated to S, which in the apo form is stabilized with respect to E,E WT SOD1 [38]. In this context, the C-terminal truncation in G127X can be seen as an allosteric inhibition mechanism to Zn binding, in that frustration is relieved in the apo native state, but Zn-binding function is lost. A similar scenario is observed for select mutants of subtilisin, a serine protease whose function is regulated by  $Ca^{2+}$  binding. In this protein, the mutation M50F preferentially stabilizes apo subtilisin relative to the holo form, while weakening calcium binding and promoting inactivation in the holo form [39].

Native frustration in apo SOD1 as a result of allosteric cooperativity in metal binding has potential consequences for the misfolding of SOD1. The premature protein, or a pro-

tein that perhaps due to an external agent has lost its metals, would show decreased thermal stability relative to one that had not undergone sequence evolution for high metal affinity. In this sense, the tight binding of Zn and Cu essential for enzymatic function of the mature protein as an antioxidant puts the premature form in additional peril for misfolding.

## Materials and Methods

A full description of the methods is given in the SI. Missense and truncation mutants of SOD1, both ALS-associated and rationally designed, were equilibrated and used for mechanical force, dynamic fluctuation, frustratometer, potential energy, and WHAM metal affinity assays. Rationally-designed truncation and missense mutants studied here include C57S/C146S, C57S 1-127, and WT sequences 1-110 and 1-140. Frustration and metal-binding allostery assays used either 22 and 24 ALS-associated mutants

respectively, or 90 glycine mutants (SI Table S3). Mechanical profiles are obtained after 20ns pre-equilibration from steered MD simulations (tether speed 2.5mm/s) in GBSA solvent with OPLS-AA/L force field parameters. Robustness checks are shown in SI Figure S15. Monte Carlo methods yield the statistical significance (error  $\approx 2.7$ kJ/mol, SI Fig. S21). Fluctuation analysis used SPC explicit solvent. Metal binding free energies are found from WHAM including post-relaxation and validation by thermodynamic cycles. Frustration calculations include protein conformations and protein-protein contacts only; i.e. metals are implicit in determining protein conformation but metal-protein interactions are not explicitly included. Frustrated contacts were calculated using the frustratometer server <http://frustratometer.tk>.

**ACKNOWLEDGMENTS.** We thank Neil Cashman, Will Guest, Ali Mohazab, Eric Mills, Paul Whitford, and Stephen Toope for helpful and supportive discussions. We acknowledge funding from PrioNet Canada, NSERC funding to defray page charge costs, and we acknowledge computational support from the WestGrid high-performance computing consortium.

- Monod, J, Wyman, J, & Changeux, J.-P. (1965) On the nature of allosteric transitions: A plausible model. *J.Mol.Biol.* 12, 88–108.
- Koshland Jr, D, Nemethy, G, & Filmer, D. (1966) Comparison of experimental binding data and theoretical models in proteins containing subunits. *Biochemistry* 5, 365–385.
- Weber, G. (1975) Energetics of ligand binding to proteins. *Adv. Protein Chem.* 29, 1–83.
- Gunasekaran, K, Ma, B, & Nussinov, R. (2004) Is allostery an intrinsic property of all dynamic proteins? *Proteins: Struct. Funct. Bioinfo.* 57, 433–443.
- Ferreiro, D. U, Hegler, J. A, Komives, E. A, & Wolynes, P. G. (2011) On the role of frustration in the energy landscapes of allosteric proteins. *Proc. Natl. Acad. Sci. USA* 108, 3499–3503.
- Daily, M & Gray, J. (2007) Local motions in a benchmark of allosteric proteins. *Proteins: Struct. Funct. Bioinfo.* 67, 385–399.
- Gardino, A, et al. (2009) Transient non-native hydrogen bonds promote activation of a signaling protein. *Cell* 139, 1109–1118.
- Plotkin, S. S & Wolynes, P. G. (2003) Buffered energy landscapes: Another solution to the kinetic paradoxes of protein folding. *Proc.Natl.Acad.Sci.USA* 100, 4417–4422.
- Christopoulos, A. (2002) Allosteric binding sites on cell-surface receptors: Novel targets for drug discovery. *Nat. Rev. Drug Discov.* 1, 198–210.
- Chiti, F & Dobson, C. M. (2006) Protein misfolding, functional amyloid, and human disease. *Annu. Rev. Biochem.* 75, 333–366.
- Tainer, J. A, Getzoff, E. D, Beem, K. M, Richardson, J. S, & Richardson, D. C. (1982) Determination and analysis of the 2A structure of copper, zinc superoxide dismutase. *J. Mol. Biol.* 160, 181 – 217.
- Bertini, I, Manganl, S, & Viezzoli, M. S. (1998) Structure and Properties of Copper-Zinc Superoxide Dismutases, *Adv. Inorg. Chem.*, ed. Sykes, A. (Academic Press) Vol. 45, pp. 127 – 250.
- Valentine, J. S, Doucette, P. A, & Zittin Potter, S. (2005) Copper-Zinc Superoxide dismutase and Amyotrophic Lateral Sclerosis. *Annu. Rev. Biochem.* 74, 563–593.
- Getzoff, E. D, et al. (1992) Faster superoxide dismutase mutants designed by enhancing electrostatic guidance. *Nature* 358, 347–351.
- Bosco, D. A, et al. (2010) Wild-type and mutant SOD1 share an aberrant conformation and a common pathogenic pathway in ALS. *Nat. Neurosci.* 13, 1396–1403.
- Forsberg, K, et al. (2010) Novel Antibodies Reveal Inclusions Containing Non-Native SOD1 in Sporadic ALS Patients. *PLoS ONE* 5, e11552.
- Chiti, F & Dobson, C. M. (2009) Amyloid formation by globular proteins under native conditions. *Nat. Chem. Biol.* 5, 15–22.
- Nordlund, A & Oliveberg, M. (2006) Folding of Cu/Zn superoxide dismutase suggests structural hotspots for gain of neurotoxic function in ALS: Parallels to precursors in amyloid disease. *Proc. Natl. Acad. Sci. USA* 103, 10218–10223.
- Elam, J. S, et al. (2003) Amyloid-like filaments and water-filled nanotubes formed by SOD1 mutant proteins linked to familial ALS. *Nat. Struct. Mol. Biol.* 10, 461–467.
- Banci, L, et al. (2005) Fully Metallated S134N Cu,Zn-Superoxide Dismutase Displays Abnormal Mobility and Intermolecular Contacts in Solution. *J. Biol. Chem.* 280, 35815–35821.
- Jonsson, P. A, et al. (2004) Minute quantities of misfolded mutant superoxide dismutase1 cause amyotrophic lateral sclerosis. *Brain* 127, 73–88.
- Grad, L. I, et al. (2011) Intermolecular transmission of superoxide dismutase 1 misfolding in living cells. *Proc. Natl. Acad. Sci. USA* 108, 16398–16403.
- Das, A & Plotkin, S. S. (2012) "Mechanical probes of SOD1 predict systematic trends in metal and dimer affinity of ALS-associated mutants". *J. Mol. Biol.*(In Press)
- Khare, S. D & Dokholyan, N. V. (2006) Common dynamical signatures of familial amyotrophic lateral sclerosis-associated structurally diverse Cu, Zn superoxide dismutase mutants. *Proc. Natl. Acad. Sci. USA* 103, 3147–3152.
- Potter, S. Z, et al. (2007) Binding of a single zinc ion to one subunit of copper-zinc superoxide dismutase apoprotein substantially influences the structure and stability of the entire homodimeric protein. *J. Am. Chem. Soc.* 129, 4575–4583.
- Schuyler, A. D, Carlson, H. A, & Feldman, E. L. (2011) Computational methods for identifying a layered allosteric regulatory mechanism for ALS-causing mutations of Cu-Zn superoxide dismutase 1. *Proteins: Struct. Funct. Bioinfo.* 79, 417–427.
- Edwards, S. A, Wagner, J, & Gräter, F. (2012) Dynamic prestress in a globular protein. *PLoS Comput. Biol.* 8, e1002509.
- Whitford, P. C, et al. (2009) An all-atom structure-based potential for proteins: Bridging minimal models with all-atom empirical forcefields. *Proteins: Struct. Funct. Bioinfo.* 75, 430–441.
- Furukawa, Y & O'Halloran, T. V. (2005) Amyotrophic Lateral Sclerosis Mutations Have the Greatest Destabilizing Effect on the Apo- and Reduced Form of SOD1, Leading to Unfolding and Oxidative Aggregation. *J. Biol. Chem.* 280, 17266–17274.
- Hörnberg, A, Logan, D. T, Marklund, S. A, & Oliveberg, M. (2007) The coupling between disulphide status, metallation and dimer interface strength in Cu/Zn superoxide dismutase. *J. Mol. Biol.* 365, 333–342.
- Banci, L, Bertini, I, Cramaro, F, Del Conte, R, & Viezzoli, M. S. (2003) Solution Structure of Apo Cu,Zn Superoxide Dismutase: Role of Metal Ions in Protein Folding. *Biochemistry* 42, 9543–9553.
- Bertini, I, Piccioli, M, Viezzoli, M. S, Chiu, C. Y, & Mullenbach, G. T. (1994) A spectroscopic characterization of a monomeric analog of copper, zinc superoxide dismutase. *Euro. Biophys. J.* 23, 167–176.
- Li, L, Guest, W, Huang, A, Plotkin, S. S, & Cashman, N. R. (2009) Immunological mimicry of PrPC-PrPSc interactions: antibody-induced PrP misfolding. *Prot. Eng. Des. Sel.* 22, 523–529.
- Cheng, H, et al. (2009) Autoinhibitory interactions between the PDZ2 and C-terminal domains in the scaffolding protein NHERF1. *Structure* 17, 660–669.
- Benson, N. C & Daggett, V. (2008) Dymaeomics: Large-scale assessment of native protein flexibility. *Prot. Sci.* 17, 2038–2050.
- Roberts, B. R, et al. (2007) Structural Characterization of Zinc-deficient Human Superoxide Dismutase and Implications for ALS. *J.Mol.Biol.* 373, 877–890.
- Museth, A, Brorsson, A, Lundqvist, M, Tibell, L, & Jonsson, B. (2009) The ALS-associated mutation G93A in human copper-zinc superoxide dismutase selectively destabilizes the remote metal binding region. *Biochemistry* 48, 8817–8829.
- Nordlund, A, et al. (2009) Functional features cause misfolding of the ALS-provoking enzyme SOD1. *Proc. Natl. Acad. Sci. USA* 106, 9667–9672.
- Bryan, P. N. (2000) Protein engineering of subtilisin. *Biochim. Biophys. Acta (BBA) - Prot. Struct. Mol. Enzymol.* 1543, 203 – 222.

# SOD1 Exhibits Allosteric Frustration to Facilitate Metal Binding Affinity (Supporting Information)

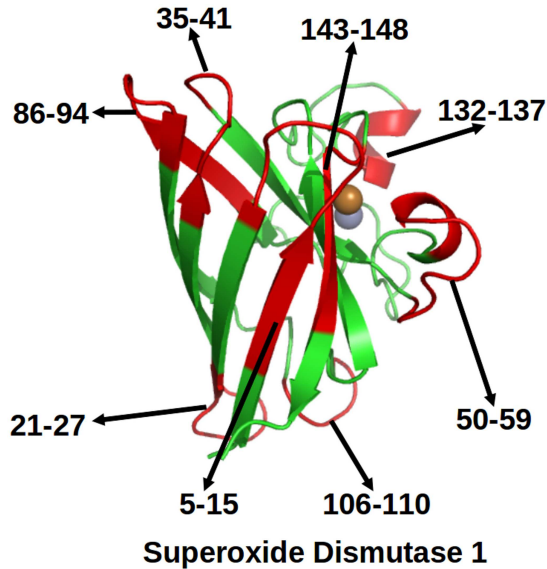
Atanu Das\* and Steven S. Plotkin\*

\*Department of Physics and Astronomy, University of British Columbia, Vancouver, Canada

## SI-text

**Work-extension profiles provide a measure of local mechanical stability, and have distance-dependent stiffness moduli.**

We performed pulling simulations on residues taken from the mid-points of the protein sequences of superoxide dismutase predicted to be either weak (referred to here as candidate epitopes) or strong (candidate anti-epitopes) thermodynamically (see Fig. S1).



(Anti)-Epitope sequence	Center residue taken	Work(5 Å)
5 – 15	10	66.1
(16 – 20)	17	91.5
21 – 27	24	58.8
(28 – 34)	31	66.3
35 – 41	38	67.1
(42 – 49)	45	83.4
50 – 59	54	85.0
(60 – 85)	73	125.0
86 – 94	90	87.9
(95 – 105)	100	97.8
106 – 110	108	69.2
(111 – 131)	121	113.6
132 – 137	135	79.4
(138 – 142)	140	99.7
143 – 148	145	72.8
(149 – 153)	151	76.6

**Fig. S1.** Ribbon representation of monomeric SOD1 structure with Cu and Zn metals shown as orange and gray spheres respectively. Candidate misfolding-specific epitopes as predicted by the algorithm of Guest, Cashman and Plotkin [1] are colored red, and their residue numbers are indicated. In the Table - Epitopes, anti-epitopes, pulling residues, and resulting work values for Cu,Zn (SS) WT SOD1.

A tethering point was placed on the  $C_{\alpha}$  atom at the center residue of a candidate epitope or anti-epitope (see Methods below), and another tethering point was placed on the  $C_{\alpha}$  atom closest to the center of mass of the protein (histidine 46). A plot of the pulling force *vs* extension for a loading rate of  $2.5 \times 10^{-3}$  m/s is shown in Figure 1(A) inset (a) of the main text, for the residues centered at the midpoints of the first candidate epitopes/anti-epitope (see Methods). The first (weak stability) epitope contains residues 5 – 15 so the  $C_{\alpha}$  atom of residue 10 is taken as a tethering point. The first anti-epitope predicted to be thermo-mechanically stable consists of residues 16 – 20 for which residue 17 is chosen as representative (see Methods).

The forces fluctuate stochastically, however the work to pull to a distance  $x$ , being the integral of the force  $W(x) = \int_0^x F(x') dx'$  results in a smooth curve (Fig. 1(A)). The work generally does not have a slope of zero as  $x \rightarrow 0$  on the length scale of  $\sim 1 \text{ \AA}$ , because of an initial small-distance nonlinear response corresponding to a steep rise in force within  $\sim 0.1 \text{ \AA}$ . That is, a force response function that appeared to converge to a non-zero force as  $x \rightarrow 0$  would correspond to a work function with linear behavior as  $x \rightarrow 0$ .

We interpret the initial steep rise in force as being due the collective effect of numerous strong bonds which seek to preserve the native structure. As distance is increased, the number of restoring interactions, and/or the magnitude of these interactions, is decreased. Thus the effective modulus of the system as calculated by  $2W(x)/x^2$  is distance dependent, and softens with increasing distance (see Methods). A plot of the effective modulus for short distances  $< 1 \text{ \AA}$  is given in inset (b) of Figure 1(A).

Previous measurements of force *vs.* extension or force *vs.* time have shown that the force converges to non-zero values at short distances or times. This is the case for ligand binding simulations [2] where the force converged to  $\sim 50 - 100 \text{ pN}$  for the shortest times, and in protein unfolding simulations [3,4] where the force converged to  $\sim 400 - 700 \text{ pN}$  at the shortest distances. These observations are consistent with the steep initial rises in the force and corresponding distance-dependent moduli that we have resolved in the present study.

It was also observed that pulling on a given residue resulted in large fluctuations in remote regions of the protein. For example pulling on residue 10 disordered  $\alpha$ -helix 2 containing residues 133-138, and pulling on residue 17 disordered  $\alpha$ -helix 1 containing residues 55-61 (Figure 1(A) inset figures).



Local mechanical strain, at least by pulling a residue, induces a non-trivial stress profile that results in induced disorder at remote regions in the protein. Such induced disorder may be a key ingredient in the propagation of misfolded SOD1 conformations in ALS, as well as other misfolding diseases propagated by template directed misfolding.

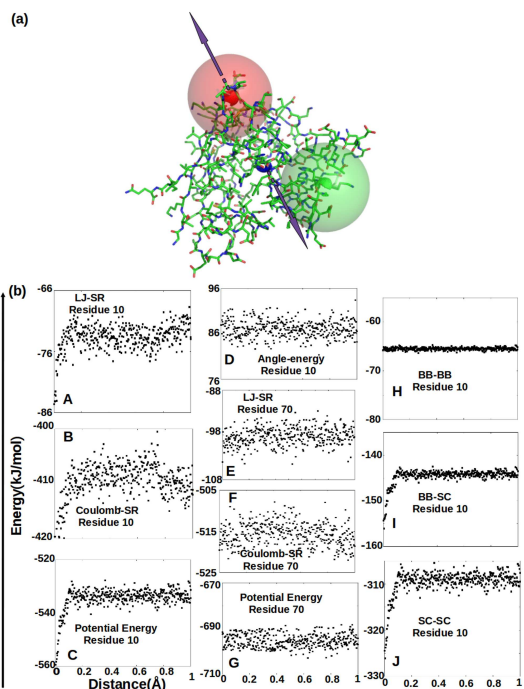
**The origin of large stiffness moduli at very short (sub-Angstrom) distances is likely due to side chain docking.** What is the origin of this highly local mechanical rigidity that gives rise to steep initial increases in force? From our pulling simulations, it was observed that the forces required to extend well-structured parts of the protein were much larger than the forces required for parts of the protein that were poorly structured or disordered. For example, in the range of extensions from  $\approx 0.1 - 0.2 \text{ \AA}$ , the force on residue 17 in  $\beta$ -strand 2 of SOD1 was  $\approx 83 pN$ , and the force on residue 10 in turn 1 was  $\approx 67 pN$ , while the force on residue 60 in the disordered Zn-binding loop of Zn-depleted SOD1 was  $\approx 52 pN$ . As an example of a residue that should lack any side-chain docking, the force on residue 133 at the disordered, non-native C-terminus of the C-terminal truncation mutant E,E G127X is  $\approx 41 pN$ . We thus investigated the phenomenon of short-range mechanical rigidity by calculating the components of the interaction energy as a tethered residue was pulled.

Figure S2(a) depicts a schematic of the simulation protocol, and Figure S2(b) shows the results. From these potential energy calculations, we see that the initial steep rise in force is due to the loss of short-range van der Waals and electrostatic interactions during the course of unfolding. The decrease in interactions is mainly between side chains (SCs) rather than backbone (Fig. S2(b) panel J): roughly 3/4 of the change in energy arises from SC-SC interactions. This effect thus appears to be due to the many-body interactions stabilizing native structures through SC-SC docking, likely formed in the latest stages of folding.

**Utility of making cumulative distribution.** In the manuscript, we have analysed the mechanical profiles mainly by constructing cumulative distributions of the work profiles, rather than the more common probability distribution measurements. The reason behind representing the work profiles in the form of cumulative distributions is that this representation gives the best way to differentiate between work profiles of two different variants of SOD1. The mechanical work profiles are too noisy to compare their relative stability from the sequence-resolved work profiles. Histograms of two work profiles also do not clearly differentiate between two different variants of SOD1 (see Figure S3). However, the cumulative distributions of the work profiles make them completely distinguishable and help to easily identify the relative order of stability among the variants.

**The mechanical profiles of Cu,Zn (SS) WT and E,E (SH) WT SOD1 are different, and are independent of the starting PDB structure used to construct them.** We can take the value of the work needed to pull a particular residue out to  $5 \text{ \AA}$  as a representation of the mechanical rigidity of that residue. This value can then be scanned across the protein sequence to obtain a mechanical profile or fingerprint for a particular SOD1 variant. Obtaining a work value for a given residue is computationally intensive however, so we take a subset of 48 residues as a “sparse sampling” of the mechanical profile, in order to compare mechanical stability between SOD1 variants. The specific residues chosen are given in the Methods section. Mechanical profiles may be compared between WT

SOD1 and various modified SOD1 proteins, including mutant SOD1 (see Figure S13), de-metallated SOD1, and disulfide-reduced SOD1.



**Fig. S2.** (Panel (a)) Schematic representation of the method of calculation of interaction energy terms shown in panel (b). We have calculated the interaction energy terms of the atoms that are within  $5 \text{ \AA}$  radius from the  $C_{\alpha}$  atom of residue 10 and 70 when residue 10 is pulled - the blue sphere indicates the  $C_{\alpha}$  of residue 46 which is the center of the protein, the small red sphere indicates the  $C_{\alpha}$  atom of residue 10 which is the tethering point, and small green sphere indicates the  $C_{\alpha}$  atom of residue 70. The arrows show the direction of pulling. The larger, semi-transparent red and green spheres have radii of  $5 \text{ \AA}$ , and enclose the atoms within  $5 \text{ \AA}$  from the respective  $C_{\alpha}$  atoms of the protein. (Panel (b)) Various terms in the potential energy as a function of distance, when residue 10 is pulled. The energies for residue 70 are investigated as a control. Analyzing individual terms in the potential energy elucidates the reason behind the initial sub-angstrom steep rise in the mechanical force. Figures A, B, and C plot the rise in short-range van der Waals energy, short-range component of the Coulomb energy, and total potential energy as a function of distance. These show a concurrent rise on the length scale of the sudden rise in the force in Figure 1(A) inset (a), main text. No such distance-sensitive change is seen for angle energies in residue 10 (figure D), or for any energies of a control residue (70) far from the pulling site (figures E,F,G). Decomposing the potential energy terms into backbone-backbone (H), backbone-sidechain (I), and sidechain-sidechain terms (J) shows that BB-BB interactions play no role, and about 3/4 of the total contribution arises from SC-SC interactions, indicating SC docking plays a dominant role in small RMSD mechanical stability.

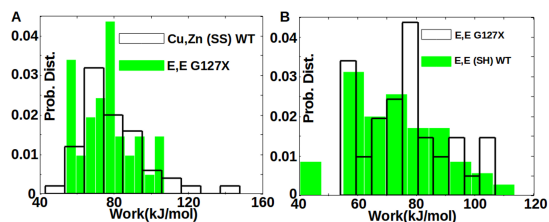


**Fig. S3.** Panel A: Probability distribution of work values of Cu,Zn (SS) WT and E,E G127X. Panel B: Probability distribution of work values of E,E G127X and E,E (SH) WT SOD1.

We first ensured that the mechanical profile obtained for a given SOD1 variant was independent of the initial conditions used in the simulations, in particular for SOD1 variants that currently have no PDB structure such as E,E (SH) WT SOD1. Equilibrated structures were generated as described in the Methods section below, and used as initial conditions for pulling simulations to generate mechanical profiles. Inset A of Figure S4 shows a plot of the mechanical scan for Cu,Zn (SS) WT SOD1, and the main panel of Figure S4 shows the mechanical scan for E,E (SH) WT SOD1.

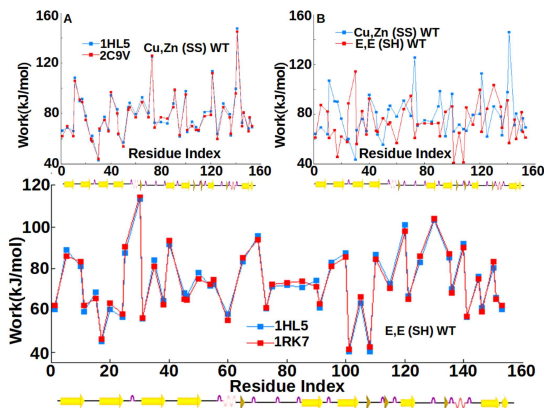


**Fig. S4.** The mechanical work profile is independent of the crystal/NMR structure used to generate the initial ensemble in a pulling simulation. The main panel shows the mechanical profile that results from 2 different constructions of the initial ensemble of E,E (SH) WT SOD1. In one construction we start from the solution structure of E,E (SS) WT SOD1, reduce the disulfide bond, and equilibrate the system before starting simulations. In another construction we start from the crystal structure of Cu,Zn (SS) WT SOD1, remove the metals and reduce the SS-bond, and then equilibrate. (Inset A) The mechanical profile obtained from 2 different crystal structures of Cu,Zn (SS) WT SOD1 (1HL5 and 2C9V), equilibrated for 20ns and then simulated as described in the Methods. Both models give the same mechanical profile to within about 2.7 kJ/mol. (Inset B) Work profiles for Cu,Zn (SS) WT and E,E (SH) WT SOD1 are seen to be significantly different, with E,E (SH) WT SOD1 generally having weakened mechanical susceptibility in various regions, but occasionally showing stiffer response in some locations.

In each case, the protein was constructed from two different initial models of the protein structure, using two different PDB structures as starting points. We found that the mechanical profile of a particular SOD1 variant was nearly independent of how that variant was constructed, reinforcing the reliability of the mechanical scan. In inset A of Figure S4, mechanical work profiles correspond to crystal structures 1HL5 [5] and 2C9V [6] of Cu,Zn (SS) WT SOD1. In the main panel of Figure S4, mechanical work profiles correspond to E,E (SH) WT SOD1, obtained by modifying either the Cu,Zn (SS) WT crystal structure 1HL5, or the NMR structure 1RK7 of E,E (SS) WT SOD1 [7]. We note that these PDB structures are equilibrated for 20 ns before any simulation measurements are taken. The mean error between SOD1 variants, as determined by the z-test described in the Methods section, is 2.7 kJ/mol. On the other hand, the standard deviation of all 48 of the work values themselves for a given variant (e.g. 1HL5) is 18.3 kJ/mol, which is a factor of about 6.8 larger than the error. The mean error between variants used to construct the same initial condition indicates the level of accuracy of the simulations, so that differences in work profiles (e.g. between mutant and WT) must generally be larger than this mean error to be significant. Inset B to Figure S4 plots the mechanical profiles of Cu,Zn (SS) WT SOD1 and E,E (SH) WT SOD1. They are seen to be significantly dif-

ferent; in particular the combination of metal depletion and disulfide reduction reduces the overall mechanical stability of several regions of SOD1. We analyze this in more detail in the manuscript.

### An implicit solvent model is sufficiently accurate to obtain the mechanical profile.

To test the accuracy of the generalized Born surface area (GBSA) implicit solvent model in determining the mechanical profile, we have performed pulling simulations on SOD1 in explicit solvent, where waters interact through the SPC force field.

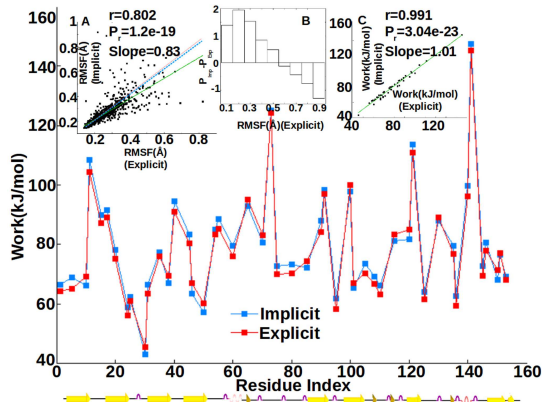


**Fig. S5.** The main panel shows that the work profiles agree between implicit and explicit solvent simulations. (Inset A) Scatter plot of the root mean square fluctuation (RMSF) for heavy atoms in the protein in both implicit and explicit solvents;  $r = 0.802$ ,  $P_r = 1.2e-19$ . Green solid line is the best fit line with a slope of 0.83. Blue dashed line is the line of slope unity, with  $y = x$ . Red dashed line is the median-fit line with an equal number of data points above and below it, and has a slope of 1.08. (Inset B) Difference in the distributions of RMSF between the implicit and explicit solvent models. This shows an enhancement of small RMSF values and suppression of large RMSF values for the implicit solvent model. (Inset C) Scatter plot of work values obtained from implicit solvent *vs* explicit solvent models; these models correlate with  $r = 0.991$ .

Inset A of Figure S5 plots the root mean squared fluctuations of heavy atoms, obtained from 20ns simulations for both implicit and explicit solvent models. The two systems have comparable thermal fluctuations, though the best fit line (green line in inset A of Fig. S5) has a slope less than unity, indicating somewhat larger fluctuations in the explicit solvent model. Interestingly however, the number of data points above and below the best fit line are 624 and 455 respectively, indicating that there are non-Gaussian fluctuations and outliers between the two models.

This skew in the data may be investigated through the distributions of RMSF, for both the implicit and explicit solvent models. These distributions are different. The difference in the distributions,  $P_{Imp} - P_{Exp}$ , as a function of RMSF, is plotted in inset B of Figure S5. This shows that the implicit solvent model overestimates small fluctuations, and underestimates large fluctuations, as compared to the explicit solvent model.

We can investigate what slope line would give equal numbers of data points above and below it, as an additional measure of the validity of the implicit solvent model. By this measure the implicit solvent model agrees much better with the explicit solvent data: the median fit line with equal numbers of data above and below it has a slope of nearly unity (slope=1.08).

The imperfect correlation between implicit and explicit solvent fluctuations prompts a comparison of the work values

in implicit and explicit solvent. A scatter plot of work values to pull the same residues to 5 Å in implicit and explicit solvent models is shown in inset C of Figure S5. Interestingly, here we see a much stronger correlation for the values of mechanical work. The mechanical work values result from a significant non-equilibrium perturbation compared to the local fluctuations in the native basin, the latter of which are apparently more sensitive to solvent conditions. A mechanical scan of 48 residues is shown in the main panel of Figure S5. Here the implicit and explicit solvent models show good agreement: the standard deviation of the difference in work profiles is about  $\approx 2.5$  kJ/mol which is less than the mean error of  $\approx 2.7$  kJ/mol obtained from using different crystal structures to set up the same initial conditions. One caveat is that the implicit solvent work values tend to be slightly higher than those of the explicit solvent: the mean of  $\Delta W$  is about 1.1 kJ/mol, so that a z-test indicates the data  $\Delta W$  arise from a gaussian distribution of mean zero only when the standard deviation of the gaussian distribution is 4 kJ/mol or larger. Overall, the data indicate that the implicit solvent model yields mechanical profiles that are as reliable as those obtained from much more time-intensive explicit SPC solvent simulations, but perhaps with modestly larger values ( $\approx 1$  kJ/mol) of work.

**A Gō model does not adequately capture the mechanical profile to sufficient accuracy.** Since the implicit-solvent model captured the mechanical profile to good accuracy, we pursued a further step in simplifying the energy function, to see if a Gō model [8] would succeed in reproducing the mechanical profile. The Gō model recipe [9] (see Methods) takes heavy atoms within 2.5 Å, and applies native contacts to them with an LJ-like 6-12 potential. The Gō recipe also attributes energy to native-like dihedral angles. The overall energy scale of all interactions is given by 1 kJ/mol times the number of atoms in the system. This recipe is intended to approximately account for all native stabilizing interactions as well as solvation free energy.

Figure S6 plots the work profiles of Cu,Zn (SS) WT SOD1, for both an all-atom implicit-solvent model and an all-atom Gō model. Perhaps surprisingly, the default energy scale in the Gō model, 1 kJ/mol times the number of atoms, captures the overall energy scale of the work profile quite well: both energy functions resulted in variation of the work from about 40 kJ/mol to about 120 kJ/mol. However, from a blind comparison of the cumulative distributions for the implicit solvent and Gō models, one would conclude they were significantly different. One can adjust the overall energy scale in the Gō model to better capture the mechanical work distribution, but the optimal value of the energy scale is not known *a priori*. Moreover, the correlation between the implicit-solvent and Gō models,  $r = 0.377$ , is not strong (Fig. S6 inset A). Increasing the overall Gō energy scale by a factor of 1.1 to improve the comparison of the cumulative distributions (inset C of Fig. S6) does not improve the correlation between work values:  $r = 0.385$ ,  $P = .007$ . The green line in inset A of Figure S6 indicates the best linear fit between the Gō and implicit solvent models. The most significant outlier on the scatter plot is residue 141, a glycine (circled data point in Fig. S6 inset A), which also can be seen to have the largest discrepancy in the mechanical profile. It has the largest work in the implicit-solvent model, and one of the smallest in the Gō model. Excluding this residue increases the correlation between the two models to 0.621 (blue line in inset A). Why is it so anomalous? The residue resides in the so called electro-

static loop, which is enriched in charged and polar residues, and coulombic energies are not explicitly treated in the Gō model, which only contains 6-12 van der Waals-like interactions.

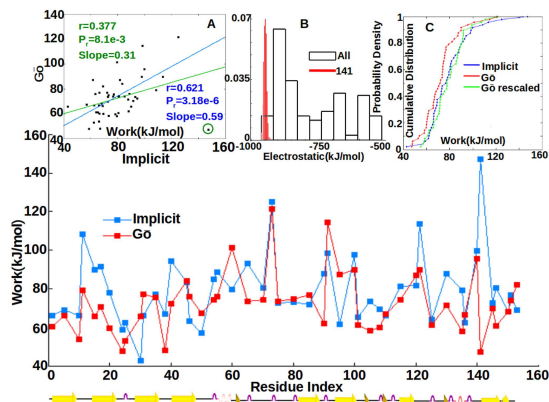


**Fig. S6.** Work profiles of Cu,Zn (SS) WT SOD1 obtained from an implicit solvent model, and a Gō model. Both models are all-atom. (Inset A) Scatter plot of the work values obtained from both models. The green line is the best fit line to the data, which has a correlation that is weak ( $r = 0.377$ ) but statistically significant ( $P = 0.008$ ). Note that the energy scales range from about 40kJ/mol to 120kJ/mol for both models. Omitting one amino acid in the electrostatic loop, residue G141 (green circled data point in the lower right of panel A), increases the correlation to 0.62 and the significance to 3e-6 (blue line). Either with or without residue 141, the slope of the line is less than unity however, indicating that stabilizing energetics are missing in the Gō model. (Inset B) Distribution of the electrostatic potential energy within a sphere of radius 5Å centered at the C $\alpha$  atom, for all residues in the monomeric protein. Residue 141 has one of the largest contributions of electrostatic energy, which explains why its work value in the implicit solvent model was much higher than that in the Gō model, which does not explicitly account for electrostatics. (Inset C) Cumulative distributions of the work values obtained from the implicit solvent (blue) and Gō (red) models. The mean work difference in the cumulative distributions between the two models is  $\approx 7$  kJ/mol. The green cumulative distribution in inset C corresponds to a Gō model that has been reweighted to have contact and dihedral energies that are 1.1 $\times$  as strong. This shifts the work distribution to larger values, but the values themselves still do not correlate well with those in the implicit solvent model:  $r = 0.385$ ,  $P = 0.007$ .

We thus investigated the electrostatic component of the energy within a sphere of radius 5Å, centered at the C $\alpha$  atom for every residue, to construct the histogram in inset B of Figure S6. The energies plotted are the mean values of the energy from an equilibrium simulation at 300K. The histogram of electrostatic energy for glycine 141 is also plotted. Indeed, residue 141 has one of the largest electrostatic contributions to its energy. This is impressive because of the small size, apolarity, and neutrality of the residue. Electrostatic contributions to protein stability, for example due to ion pairs or partial charges in either close proximity or in low dielectric environment, may be poorly accounted for in Gō models.

**The mechanical profile accurately reflects the free energy profile of the protein.** The work to pull a given C $\alpha$  atom to 5Å is a non-equilibrium measurement of mechanical stiffness, and one can ask whether it accurately represents the thermodynamic stability of that region. To address this question, we obtained the free energy to separate each of the 48 C $\alpha$  atoms used in the mechanical pulling simulations by 5Å. The procedure for obtaining the free energy is described in the Methods section. Figure S7 plots the work values for all 48 residues used in the pulling simulations of Cu,Zn (SS) WT SOD1, *vs.* the free energy values for the corresponding residues as obtained from the weighted histogram analysis

method (WHAM). The correlation coefficient is 0.96, indicating that the relative mechanical rigidity can be used to predict the relative thermodynamic stability.

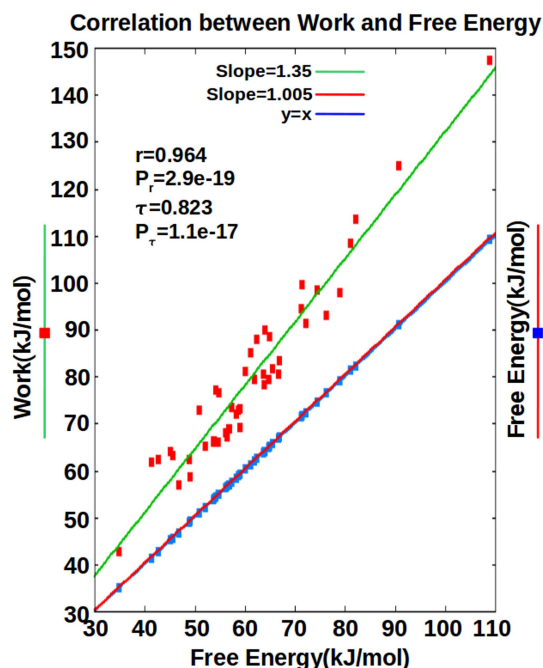


**Fig. S7.** (Red squares) Work to pull a given residue to 5Å vs the free energy change for a fluctuation to separate that residue by 5Å, for Cu,Zn (SS) WT SOD1. Free energies on the abscissa are obtained from umbrella sampling and the weighted histogram analysis method (WHAM). Both work values and free energies, for the red squares, are obtained using a slow pulling speed of  $2.5 \times 10^{-3}$  m/s. All 48 residues used in the pulling simulations are shown. The correlation between work and free energy values is very strong,  $r = 0.96$ . For the pulling rates used in our study, the work values are about  $1.3 \times$  as large as the free energies, and the slope of the best fit line is 1.35. Blue squares: WHAM-derived free energy changes, as obtained from pulling simulations at two different pulling rates: The abscissa values give the free energy for a pulling rate of  $2.5 \times 10^{-3}$  m/s as above, the ordinate values have a pulling rate of 10 m/s. In addition to a near perfect correlation, the slope defined by the best fit line to the two sets of data is nearly unity (purple line), and the data is well-fit by the line  $y = x$  (cyan line) indicating that the free energy values are independent of the pulling speed used to obtain the initial data, and thus have been reliably determined.

The work values are higher than the free energy values however, by a factor of about  $\langle W/F \rangle \approx 1.3$ . The average mechanical work, as a non-equilibrium measurement, always exceeds the free energy change that would be due to rare equilibrium fluctuations.

Since a faster pulling rate results in more deformation of the protein, different pulling rates can in principle result in initial conditions that, after umbrella sampling and WHAM, give different free energy profiles. We checked this by performing WHAM calculations at two different pulling speeds,  $2.5 \times 10^{-3}$  m/s and 10 m/s. The faster pulling speed results in more deformed protein structures that were used as initial conditions, however, each initial condition is always equilibrated for 10 ns in an umbrella potential as described in the Methods, which should remove most or all initial deformation effects. The free energy values thus obtained did not depend on the initial pulling speed used to generate the initial conditions for the WHAM protocol: they are within a factor of 1.005. We thus used relatively fast pulling speeds of 10 m/s to

obtain initial conditions used to calculate free energies from the WHAM method.

**The mechanical profile obtained from about 40 residues captures the distribution of work values for a given SOD1 variant to sufficient accuracy.** Inset A of Figure S8 shows the mechanical work profile to pull residues to 5Å, for every residue between the N-terminus and residue 40. Residues from the original set of 48 are shown in red, others in blue. The values deviate significantly residue to residue, with a correlation length less than the putative value of  $\sim 5$  amino acids corresponding to the original data set. By calculating the residue-residue correlation function of the work  $\langle W_i \cdot W_{i+n} \rangle$  and fitting to  $\exp(-n/\ell_p)$ , the sequence correlation length is found to be  $\approx 2.83$ . The work values found from the mechanical scan using the original sampling of 48 residues should thus not be interpreted as consensus values for the corresponding regions.

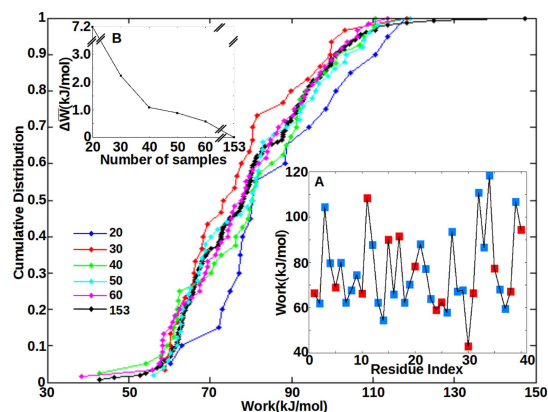


**Fig. S8.** (Inset A) Mechanical work profile to pull residues to 5Å, for every amino acid between the N-terminus and residue 40. Residues from the original set of 48, discussed in the Methods subsection on residues used for mechanical scans, are shown in red, others in blue. Work values deviate significantly residue to residue, with a sequence correlation length  $\ell_p \approx 2.83$ , as defined through  $\langle W_i \cdot W_{i+n} \rangle \propto \exp(-n/\ell_p)$ . The work values found from the mechanical scan using the original set of 48 residues should thus not be interpreted as consensus values for the corresponding regions. (Main panel) Cumulative distributions of the work values for Cu,Zn (SS) WT SOD1, constructed simply by rank ordering the work values and plotting the fraction of the total number vs the work. Each cumulative distribution corresponds to a specific number of data points (work values) as given in the legend, which are randomly selected from the total set of 153 data points. As the number of data points is increased, the cumulative distribution converges to that for the full data set. The average deviation of work values is plotted in inset B. By 40 data points, the cumulative distribution has converged to within  $\approx 1.08$  kJ/mol of the full 153-data point distribution. By 50 data points, it has converged to within  $\approx 0.88$  kJ/mol of the full distribution.

One can ask if the mechanical scan still has utility then. The main panel of Figure S8 shows a cumulative distribution of the work values for Cu,Zn (SS) WT SOD1, which is constructed simply by rank ordering the work values and plotting the number vs the work, subsequently normalizing to unity. Several curves are shown: each curve corresponds to a given number of data points randomly selected from the total set of 153 data points. As the number of data points is increased, the distribution converges to that containing the full data set. Inset B of Figure S8 plots the mean deviation in work values between cumulative distributions. After about 40 data points, the cumulative distribution converges to within about 1.08 kJ/mol of the full distribution using 153 data points. This deviation is smaller than the deviation in work values obtained from different starting PDB structures (see above

subsection “The mechanical profiles of Cu,Zn (SS) WT ..” and Fig. S4). That is, if one constructs cumulative distributions from the work values in Figure S4, the mean work difference between cumulative distributions is  $\approx 1.2$ kJ/mol. The data set used for our analysis, given in the Methods section, contains 48 residues, and has a mean deviation from the 153-residue cumulative distribution of about 0.9 kJ/mol.

We found that many discrepancies of SOD1 variants from WT were difficult to disentangle from the work profile, but often emerged naturally from the cumulative distribution. Mechanical scans were thus used to construct the cumulative distributions, which then allowed us to distinguish stabilizing energetics in various forms of mutant SOD1. For example, we find below that the cumulative distribution is different for differently metallated variants of SOD1 (Figure S14).

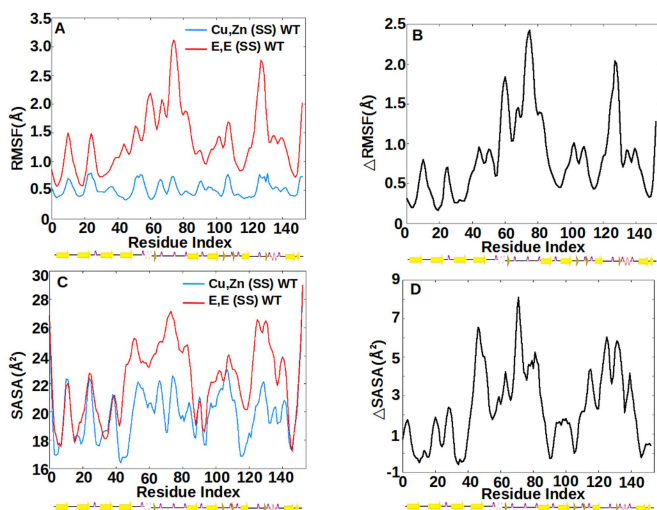


**Fig. S9.** Conformational disorder in the absence of metals, as obtained from equilibrium simulations, is largest in Zn-binding and electrostatic loops. Comparison of root mean squared fluctuations (RMSF) (A,B) and solvent accessible surface area of backbone amides ( $SASA_N$ ) (C,D), for Cu,Zn (SS) WT and E,E (SS) WT SOD1. Results are averaged over a 20 ns equilibrium simulation trajectory. Panels A and C plot the respective quantities for both proteins, and panels B and D plot the differences between E,E (SS) WT and Cu,Zn (SS) WT proteins, i.e. the change in RMSF or  $SASA_N$  upon loss of metals. Both quantities indicate substantial increase in dynamic disorder and loss of native structure in loops IV and VII, and to a lesser extent loop VI, upon loss of metals.

**Equilibrium dynamical results.** Removing metals from WT protein results in substantially increased dynamical fluctuations (RMSF) in loops IV (ZBL) and VII (ESL), and to some extent loop VI (Figure S9). The RMSF of Cu,Zn(SS) WT and E,E(SS) WT, along with their difference,  $\Delta$ RMSF, are shown in Figures S9A,B. Loops IV and VII also show increased solvent accessible surface area of backbone amide nitrogen ( $SASA_N$ ) upon loss of metals (Fig. S9 panels C,D).

The dynamic effects of fluctuations between E,E(SH) and G127X seen in Figure 2C of the main text are not recapitulated in backbone amide solvent exposure: loop IV of E,E (SH) WT SOD1 is not significantly more solvent exposed than loop IV in E,E G127X, and the N terminus of E,E G127X from strand  $\beta$ 7 onwards is more solvent exposed than the corresponding residues in E,E (SH) WT SOD1 (Fig. S10).

The profile of potential energy can be obtained by finding the potential energy within a sphere of radius  $8\text{\AA}$ , centered about a given  $C\alpha$  atom, and then varying the  $C\alpha$  index along the sequence. Consistent with the increased mechanical sta-

bility of G127X with respect to E,E(SH) WT (Fig. 1B), the potential energy profile of G127X is generally more stabilized than that of E,E(SH) WT (Fig. S11).

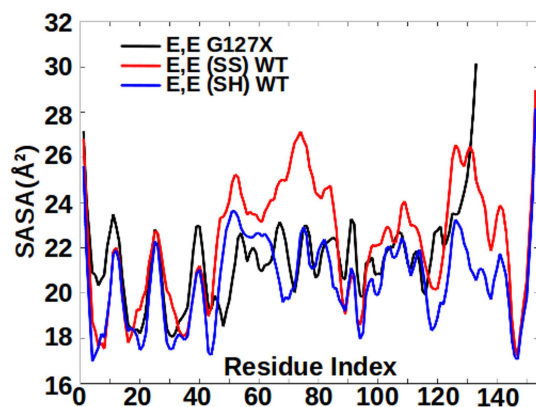


**Fig. S10.** SASA of backbone amide nitrogen atoms, from equilibrium simulations of E,E G127X, E,E(SS) WT and E,E(SH) WT SOD1.

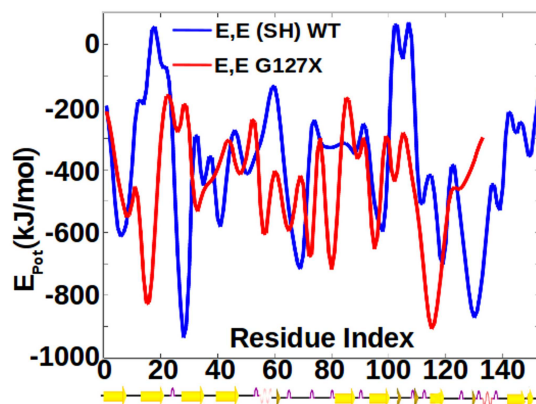


**Fig. S11.** Interaction potential energy between all atoms within an  $8\text{\AA}$  sphere of the  $C\alpha$  atom of each residue, for E,E(SH) WT SOD1 and E,E G127X SOD1.

**Comparison of metal binding free energy, thermodynamic stability, and mechanical stability.** The thermodynamic stability of the E,E(SS) monomer for several SOD1 mutants has been obtained previously by Oliveberg and colleagues [10]. The free energy difference between WT and mutant free energy of unfolding is plotted in Figure S12. As well, the change in average mechanical work values, from WT to mutant, is plotted in the same figure. The work values have been normalized by a factor of 1.35, the slope of Figure S7, to convert work values to effective free energies. Finally, the difference in metal binding free energy, WT minus mutant, for both Cu and Zn, is plotted in the same figure. All free energy changes are positive and between 1-25 kJ/mol. However, there is no significant correlation between any of these quantities, with the exception of the binding free energies of Cu and Zn ( $r = 0.91$ ,  $p = 6.6e-4$ ).

**Cumulative distributions of mechanical work for an ALS-associated mutant.** Figure S13 shows the cumulative distributions of mechanical work for both WT SOD1 and A4V, for several different post-translational modification (PTM) states.

The Cu,Zn(SS) mechanical stabilities of WT and A4V are very similar, except for the weaker regions. In contrast, the E,E(SS) protein is substantially mechanically destabilized upon mutation, and the E,E(SH) protein is even further mechanically destabilized upon mutation. Interestingly, over much of the distribution E,E(SH) WT is stabilized with respect to E,E(SS) WT. This stabilization is also observed by examining the change in potential energy upon disulfide reduction [11].

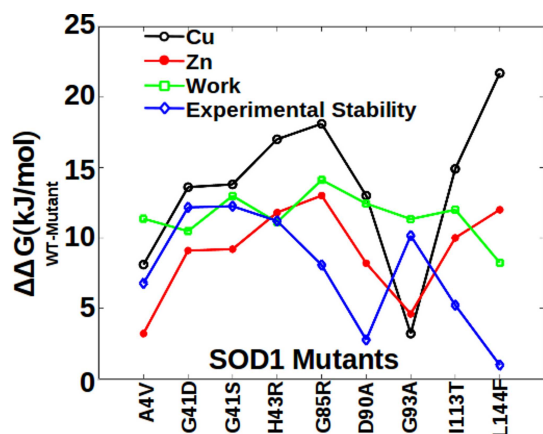


**Fig. S12.** (Black) Difference in free energy of Cu binding, WT minus mutant, (Red) Difference in free energy of Zn binding, WT minus mutant, (Green) Difference in average mechanical work values, WT minus mutant. The work values have been normalized by the slope of Figure S7 to convert them to effective free energies. (Blue) Difference in experimental thermodynamic free energy of unfolding [10], WT minus mutant.

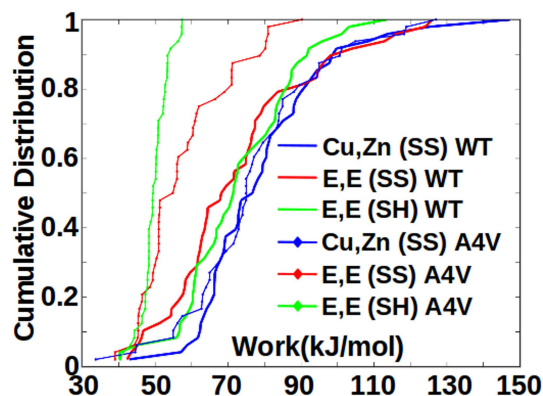


**Fig. S13.** Cumulative distributions of work values for non-post-translationally modified (PTM) variants of WT SOD1, i.e. those missing metals and/or disulfide bond. Cumulative distributions of A4V SOD1 in various PTM states are also shown.

The change in mechanical stability upon mutation for the E,E(SH) state is in contrast to the change in mechanical stability upon truncation for G127X (Figure 1B, main text). The mutations are quite different- one replaces an Alanine with a Valine and the other more drastically removes 20 residues and mutates 6 C-terminal residues.

**Cumulative distributions of WT SOD1 PTM variants.** Figure S14 shows the cumulative distributions of Cu,Zn(SS) SOD1 along with several WT SOD1 PTM variants, including E,Zn(SS), Cu,E(SS), Cu,Zn(SH), and E,E(SS) WT. Compar-

ing the mechanical destabilization of the premature variants with Cu,Zn(SS) SOD1, we see that E,E(SS) SOD1 is the least mechanically stable. Comparing individual PTM states, the loss of Zn results in the largest destabilization, followed by disulfide reduction, followed by Cu depletion.

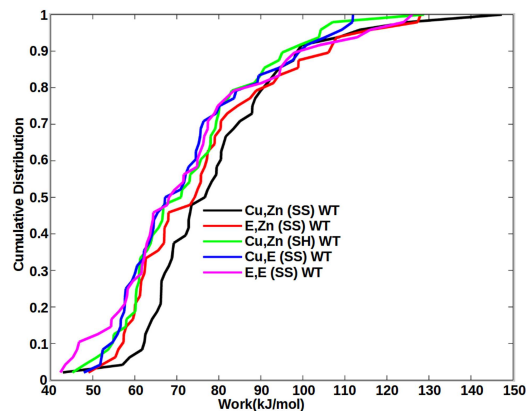


**Fig. S14.** Cumulative distribution of work values for various PTM states of WT SOD1, as indicated in the legend.

**ALS-associated mutants.** ALS-associated mutants considered in the main text were: A4V, W32S, G37R, L38V, G41D, G41S, H43R, H46R, H46R/H48Q, T54R, D76Y, H80R, G85R, D90A, G93A, G93C, I113T, G127X, D124V, D125H, S134N and L144F.

**Robustness tests of the results.** In the simulations, mechanical fingerprints were determined at  $T = 300K$ , and pulling speed  $v = 2.5mm/s$ ; both numbers are comparable to those in AFM experimental assays. The pulling distance  $\Delta x = 5\text{\AA}$  was taken to represent a significant perturbation from the native structure, but not so much so as to globally unfold the protein. To test the robustness of our results to varying external conditions, we have taken one of our conclusions, namely that E,E C57S 1-127 SOD1 is mechanically stabilized with respect to E,E C57S/C146S 1-153 SOD1 (see Figure 1D main text), and we have varied temperature, pulling speed, and pulling distance. Temperature was increased to 310K, pulling speed was altered to  $v = 1.5mm/s$  and  $4mm/s$ , and pulling distance was altered to  $\Delta x = 3, 4, 6$  and  $7\text{\AA}$ . The results are summarized in Figure S15.

Panel A of Figure S15 is at the conditions used throughout our analysis, and reproduces Figure 1D of the main text. Increasing the temperature to biological temperatures ( $T = 310K$ ) rather than lab temperatures preserves the conclusion and only slightly reduces the statistical significance. Decreasing or increasing the pulling speed to the values noted above tends to decrease or increase all work values by 2-3kJ/mol, but preserves the conclusion and leaves the significance nearly unchanged. Panels E-H of Figure S15 show increasing pulling distance  $\Delta x$  from  $3\text{\AA}$  to  $7\text{\AA}$ . The conclusions are preserved for all distances, and the statistical significance of the conclusion increases with increasing distance pulled. Taken together, the above tests indicate that the conclusions in the manuscript are robust to varying external conditions.

**Work values projected on SOD1 structure.** A mechanical scan was performed on Cu,Zn(SS) WT SOD1 for every  $C\alpha$  atom, and the work values were then projected on the native protein structure in Figure S16 panel A. As mentioned in the text, the correlation length of the work values along the se-

quence is about 3, so the projection color-coded by work value is discontinuous. Applying to the work values a simple tent-shaped smoothing function that smoothes over 5 residues gives the plot of Figure S16 panel B. This shows that for example parts of loops IV and VII are mechanically more rigid than some beta sheets, indicating significant stabilization by the presence of the metals.

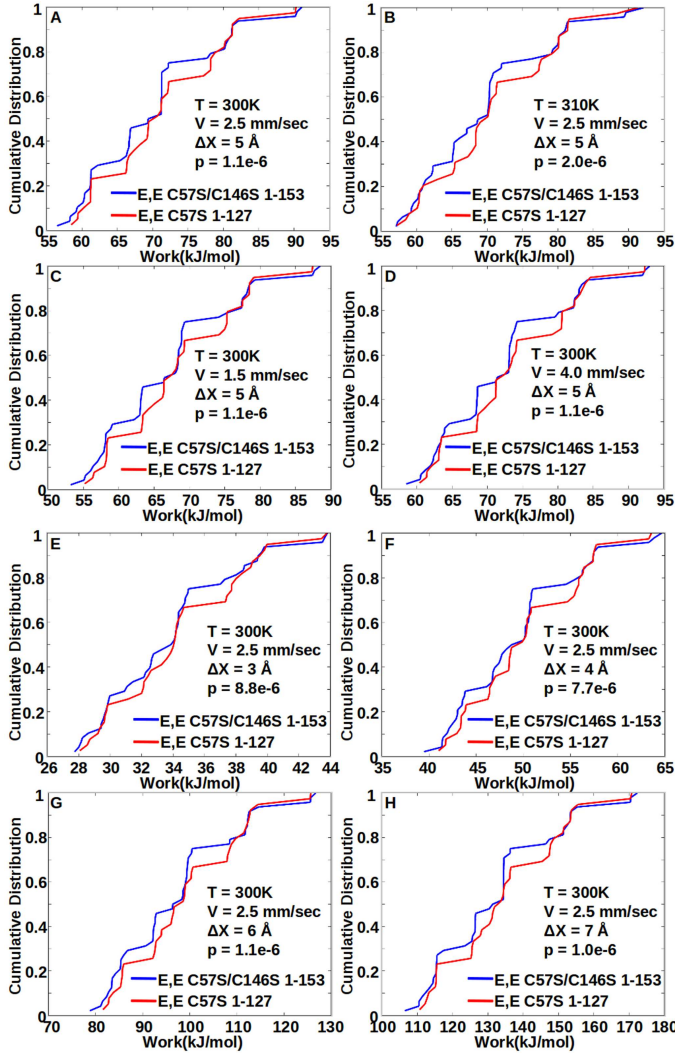


**Fig. S15.** Cumulative distribution of mechanical profiles showing E,E C57S 1-127 SOD1 is mechanically stabilized with respect to E,E C57S/C146S 1-153 SOD1 (see Figure 1D main text). Temperature  $T$ , speed  $v$ , extension  $\Delta x$ , and statistical significance of the result  $p$  as defined in the Methods below, are given for each panel. (Panel A) Assay done at conditions generally used in the main text. (Panel B): Same as panel A but at  $T = 310\text{K}$ . (Panels C,D): Same as panel A but at pulling speeds  $v = 1.5\text{mm/s}$  and  $4\text{mm/s}$ . (Panels E-H): Same as panel A but at pulling distances 3,4,6 and 7 Å. Statistical significance monotonically increases with pulling distance.

**Frustratometer analysis of a non-ALS related alanine scan of SOD1.** Figure S17 shows the results frustratometer analysis for both Cu,Zn(SS) SOD1, and E,E(SS) SOD1. The mean number of highly frustrated contacts for each variant is 2.2 and 2.45 respectively, indicating that the E,E(SS) state is more frustrated by about 38 contacts. In the main text we used frustratometer analysis [12] to show that more frustration was present in the E,E(SS) state of SOD1 than the Cu,Zn(SS)

state, by showing that upon mutation, more highly frustrated contacts were introduced in the Cu,Zn(SS) state, but frustration was removed by mutation in the E,E(SS) state. A set of 22 ALS-associated mutations were taken. Here, we check that the conclusion is general- not restricted to ALS-associated mutation- by examining the effects of 30  $X \rightarrow A$  mutations. An alanine scan across the sequence is taken, wherein every 5th residue in the SOD1 sequence is mutated to alanine if (1) it is not an alanine in the WT sequence and (2) the mutation to alanine does not lead to an ALS-associated mutant. When we encountered alanine in the WT sequence (residue 55, 60, 95, 140 and 145), we took either the previous or the next residue for our analysis as indicated below. As well, D90A is an ALS-associated mutation, so for this case we chose residue 91, i.e. K91A.

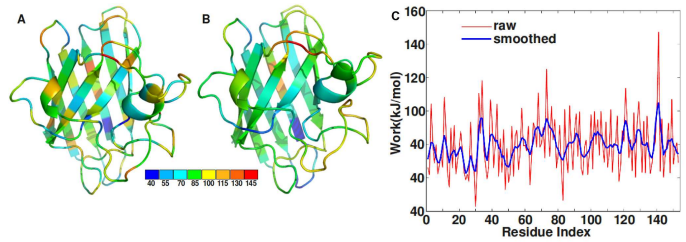


**Fig. S16.** (Panel A): Work values to pull all 153 residues to 5 Å for Cu,Zn(SS) WT SOD1, projected on the native SOD1 conformation - work values increases from blue to red. The very low correlation length of work values along the primary sequence is evident from the discontinuity of the color scheme. (Panel B): A smoothed work profile was generated from the all-residue work profile used in panel A and projected on the SOD1 conformation. (Panel C) The raw and smoothed work values as a function of sequence index.

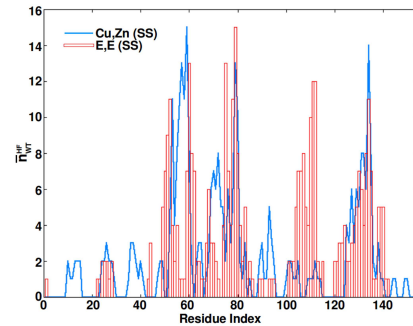


**Fig. S17.** Mean number of highly frustrated contacts in the Cu,Zn(SS) and E,E(SS) states of WT SOD1, as a function of residue index.

The 30 residues mutated to alanine are: 5,10,15,20,25,30, 35,40,45,50,56,59,65,70,75,80,85,91,96,100,105,110,115, 120,125, 130,135,139,144 and 150. We again took 50 snapshots from the equilibrium simulations of each protein to calculate the ensemble average of highly frustrated contacts  $\bar{n}^{HF}$ . We performed frustratometer analysis for each Cu,Zn(SS) or E,E(SS) alanine mutant, and calculated the difference in number of highly frustrated residues between WT SOD1 and the alanine mutant as a function of sequence index  $i$ :  $\bar{n}_{X \rightarrow A}^{HF}(i) - \bar{n}_{WT}^{HF}(i)$ . We then averaged this quantity over all alanine mutants,  $\langle \bar{n}_{X \rightarrow A}^{HF}(i) \rangle_X - \bar{n}_{WT}^{HF}(i) \equiv \langle \bar{n}^{HF} \rangle_{MUT} - \bar{n}_{WT}^{HF}$ , and plotted the result in Figure S18, panel A as a function of sequence index.

Upon mutation to alanine at the sequence locations above, the number of highly frustrated contacts increased on aver-

age by 9 for Cu,Zn(SS) SOD1 and decreased on average by 29 for E,E(SS) SOD1. This indicates that mutations which normally increase frustration in the Cu,Zn(SS) state of WT SOD1 generically decrease frustration in the WT E,E(SS) state. This recapitulates the findings in the main text for ALS-associated mutations, and supports the conclusion that the E,E(SS) state is frustrated.

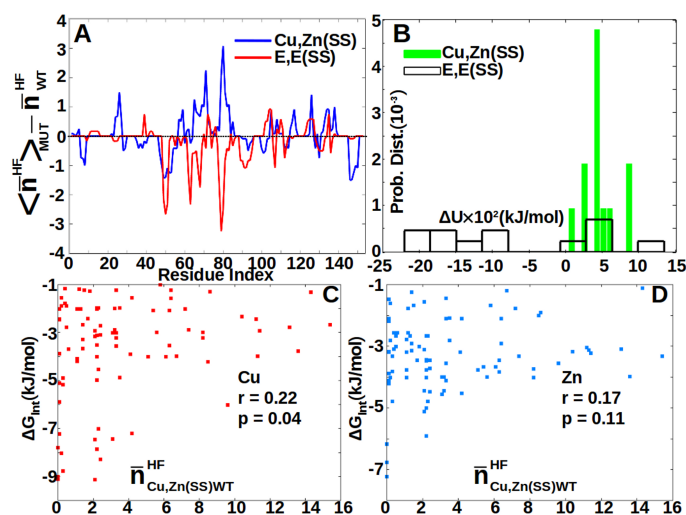


**Fig. S18.** (Panel A) The number of frustrated contacts within a sphere of radius 5Å centered on each  $C_{\alpha}$  atom, is found as a function of residue index,  $n^{\text{HF}}(i)$ . Ensemble averages are taken from 50 snapshots in an equilibrium simulation to obtain  $\bar{n}^{\text{HF}}(i)$ . This is done for both the Cu,Zn(SS) state and the E,E(SS) state, for both the WT sequence, and for 30 alanine mutants (Table S3). The 30 alanine mutant sequences are averaged to obtain the ensemble and mutant averaged number of contacts as a function of residue index  $i$ ,  $\langle \bar{n}^{\text{HF}}(i) \rangle_{\text{MUT}}$ . Plotted is the difference between  $\langle \bar{n}^{\text{HF}}(i) \rangle_{\text{MUT}}$  and the corresponding numbers for the WT sequence  $\bar{n}^{\text{HF}}_{\text{WT}}(i)$ . A positive number would indicate an increase in frustration upon mutation. Cu,Zn(SS) state is shown in blue and has an average of +9 contacts. E,E(SS) state is shown in red and has an average of -29 contacts. (Panel B) Distribution of the thermal average potential energy change upon mutation,  $\Delta \bar{U}_{X \rightarrow A}$ , for the 30 alanine mutants given in the text. Distributions for both the Cu,Zn(SS) state and the E,E(SS) state of SOD1 are shown. (Panel C) Scatter plot of the interaction free energy of a given residue's side chain with Cu, vs. the mean equilibrium number of highly frustrated contacts that residue has in the Cu,Zn(SS) state of WT SOD1. The scatter plot shows essentially no correlation. (Panel D) Same as Panel C, but for the interaction free energy with Zn. The scatter plot again shows no correlation.

**Potential energy analysis of a non-ALS related alanine scan of SOD1.** We have also calculated the difference in potential energy upon mutation, for ALS-associated mutants in the main text, and the 30 alanine mutants described above (Table S3). The procedure for calculating the potential energy change upon mutation is described in the Methods. The potential energies, averaged over 50 equilibrium conformations, are obtained both before and after mutation, and the difference obtained as  $\Delta \bar{U}_{X \rightarrow A}$ . This difference is obtained in both the Cu,Zn(SS) and E,E(SS) forms of SOD1. Plotted in Figure S18, panel B are the distributions of  $\Delta \bar{U}_{X \rightarrow A}$  over the above 30 non-ALS associated alanine mutations, for the both the Cu,Zn(SS) and E,E(SS) forms of SOD1. The same quantities are plotted in Figure 4B of the main text for 22 ALS-associated mutations. In Figure S18, panel B, we see that all 30 mutants raise (penalize) the potential energy of Cu,Zn(SS) SOD1, while most of the 30 mutants lower the potential energy of E,E(SS) SOD1. These findings are consistent with those in the main text, and indicate that the results that obtained for

ALS-associated mutants are also common to non-ALS SOD1 mutants, and so are a generic feature of SOD1.

**Correlation between metal interactions and frustration, and metal interactions and distance.** Frustratometer analysis of the equilibrium E,E(SS) state of WT SOD1 shows that 90 residues have at least 1 highly-frustrated contact (Fig. S17). The mean number of highly-frustrated contacts of each of these residues,  $\bar{n}^{\text{HF}}_{\text{E,E(SS)}}$ , may be compared with the interaction free energy of that residue with the metal  $\Delta G_{\text{int}}$ . The interaction free energy is obtained from metal extraction as described in the main text and in the Methods below. This analysis directly tests the correlation between the degree of frustration of a residue, and that residue's involvement in binding metals. Figure 3, panels B and C of the main text show a strong correlation between metal interaction free energy and the frustration of a particular residue in the E,E(SS) state: the more frustration a residue has, the stronger its interaction with the metals. As a control test, the metal interaction free energy of a given residue may be compared with its number of highly-frustrated contacts in the Cu,Zn(SS) state. Here we see no correlation for either Cu or Zn (Fig. S18, panels C,D). Hence, on a residue by residue basis, frustration in the apo state of SOD1 facilitates metal affinity for both Cu and Zn.

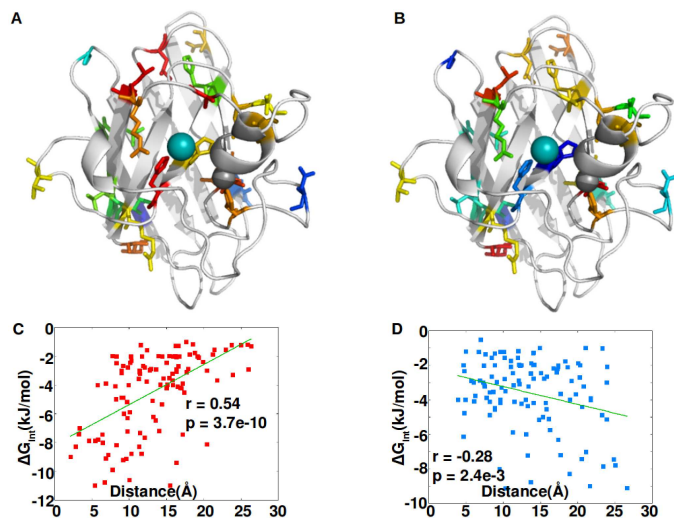


**Fig. S19.** Panel (A): Residues color-coded by interaction energy with the Cu ion (depicted as a cyan sphere). The extent of interaction is strongest in magnitude for red colored residues and decreases to blue. Panel (B): same as (A) for the Zn ion (depicted as a grey sphere). Panel (C): Interaction energy with Cu correlates with the distance of the residue from the Cu ion; residues in close proximity more strongly interact with the metal. Panel (D): Interaction energy with Zn does not correlate with distance of the residue to the Zn ion, indicating non-local allosteric effects.

The distance-dependence of the interaction free energy between a residue and either Cu or Zn was investigated in Figure 5 of the main text. Results were shown for the 24 mutants listed in Table S3. When the dataset corresponding to the 90 residues with at least one highly frustrated contact is used (Table S3), the general result remains true that allosteric regulation for metal affinity is significantly correlated with the proximity of a residue to the Cu binding site, but not with the proximity of a residue to the Zn binding site (Fig. S19). There is more scatter with this larger dataset (but also selective to only include frustrated residues) in the plot measuring correlation between interaction free energy and distance to the Cu, and the correlation decreases somewhat from that in



the main text. The conclusion remains true that the affinity for Zn is imposed collectively across the whole protein.

**Relationship between mechanical work, fluctuations, potential energy, and frustration.** In Figure S20, we plot the cumulative work distribution, RMSF, time-resolved change in potential energy after mutation, and frustratometer results for the ALS-associated mutants studied here: G127X and A4V.

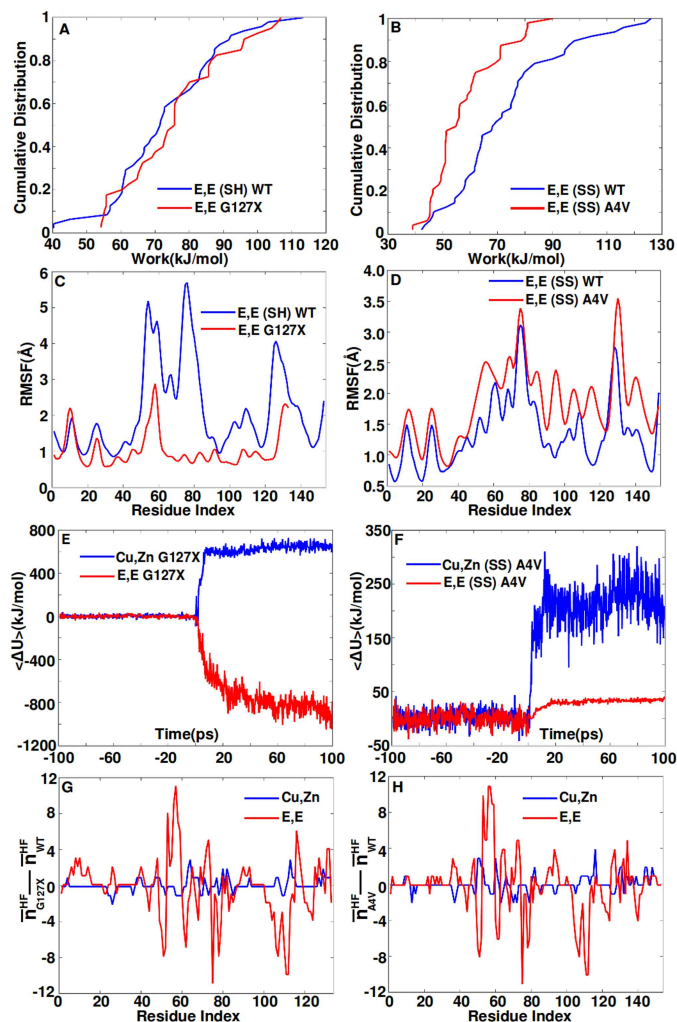


**Fig. S20.** Panel (A): Cumulative distribution of work values to pull residues to 5Å, for E,E G127X and E,E(SH) WT. Panel (B): same as (A), for E,E(SS) A4V and E,E(SS) WT. Panels (C,D): RMSF values as function of residue index, for the same proteins in Panels (A,B). Panels (E,F): time-resolved change in total potential energy after mutation, from E,E(SH) WT  $\rightarrow$  E,E G127X and Cu,Zn(SH) WT  $\rightarrow$  Cu,Zn G127X (panel E) and from E,E(SS) WT  $\rightarrow$  E,E(SS) A4V and Cu,Zn(SS) WT  $\rightarrow$  Cu,Zn(SS) A4V (panel F). Panel (G): Difference in the number of highly-frustrated contacts for each residue, G127X - WT, for Cu,Zn(SH) and E,E(SH) variants. Panel (H): Same difference as in (G), for A4V - WT, for Cu,Zn(SS) and E,E(SS) variants.

These two mutants show different behavior: The cumulative distribution of work values shows that E,E G127X is stabilized with respect to E,E(SH) WT (Fig. 1B in the main text and Fig. S20A). The mechanical stability of A4V shows the opposite effect however (Fig.s S14 and S20B): the mutation softens the protein.

The dynamic fluctuations are consistent with the work-value analysis: the fluctuations are reduced upon mutation for G127X (Fig.2C in main text and Fig. reffigcompareC), but enhanced for A4V (Fig. reffigcompareD). Likewise, the total potential energy in the apo protein decreases upon mutation for G127X (Fig. S20E) but increases upon mutation for A4V (Fig. S20F). The potential energy increases in the holo protein for both mutants.

The frustratometer analysis indicates that the frustration increases in the holo protein for both mutants, 5 contacts for G127X and 4 contacts for A4V. However for the apo proteins, the number of highly frustrated contacts in E,E G127X decreases from E,E(SH) WT by 16 contacts on average, and the number of highly frustrated contacts in E,E G127X decreases from that in E,E(SS) WT by 35 contacts. For E,E(SS) A4V, frustration is decreased from that in E,E(SS) WT by 31 contacts. Thus frustration decreases from the E,E(SS) state slightly more in G127X than in E,E(SS) A4V. A general analysis of the decrease in potential energy and frustration for apo mutants, along with the results from their individual mechanical scans, is an interesting topic for future work.

## Methods

**Steered molecular dynamics simulations.** Steered molecular dynamics (SMD) using constant-velocity moving restraints was used to simulate the action of moving AFM cantilever on a protein. The general procedure used two tethering points for the pulling simulations. In our study of SOD1 monomer, one tether was placed at the position of the alpha carbon closest to the center of mass of the protein (generally  $C_{\alpha}(46)$ ), and another tether was placed on the alpha carbon of a particular amino acid to be pulled on. To implement a mechanical stability scan across the surface of the protein, every 5th amino acid along with the first and last residues was selected for a pulling simulation. This coarse-grains the mechanical profile, so that the work values obtained are a sampling of the work values for all residues.

SMD simulations [13,14,15,16] were performed in GRO-MACS to monitor the forced unfolding of SOD1 variants. An all-atom representation of the protein was used, with OPLS-AA/L parameters [17,18], and a generalized Born surface area (GBSA) implicit solvent model was used, with dielectric constants of the protein and solvent taken to be 4 and 80 respectively. The Onufriev-Bashford-Case (OBC) algorithm was used to calculate Born radii [19]. The phenomenological surface tension coefficient used in calculating solvation free energies was 0.005 kcal/mol/(Å<sup>2</sup>) [20]. The LINCS algorithm was applied to constrain all bond lengths that contained a hydrogen atom [21].

Prior to simulation, energy was minimized using a steepest descent algorithm to remove any potential steric clashes. Simulations were carried out with an integration time-step of 2 fs and coordinates were saved after every 100 ps. The long-distance cut-off used for non-bonded interactions was 14 Å for both Electrostatic and van der Waals (VDW) interactions. A cubic simulation box with periodic boundary conditions was used, with size such that all protein atoms were initially at least 20 Å from any cubic face. For every SOD1 variant protein considered, a simulation was run for 20 ns to equilibrate the protein before any pulling simulations were performed and data was collected.

Because only moderate deformations were required to construct mechanical force-extension curves, a very slow pulling speed (for simulations) of  $2.5 \times 10^{-3}$  m/s was admissible. This speed is comparable to those used in AFM experiments [22], and is 400 – 8000× slower than the speeds generally used in

simulations [23,24,25]. The spring constant of the simulated AFM cantilever was taken to be  $5 \text{ kJ/mol/\AA}^2$ . The average  $F(x)/x$  values from the epitope pulling simulations e.g. for residues 10 and 17, in the extension range of 1-5  $\text{\AA}$ , are 5.1 and 7.3  $\text{kJ/mol/\AA}^2$  respectively, indicating that the protein effective spring constant is comparable to the cantilever spring constant. The average modulus as determined by  $2W(x)/x^3$  between 1 and 5  $\text{\AA}$  is 7.72 and 10.35  $\text{kJ/mol/\AA}^2$  for residues 10 and 17 respectively. The average modulus between 0 and 1  $\text{\AA}$  is much higher: 67.08 for residue 10 and 91.46 for residue 17 in the same units. Each pulling simulation ran until the change in distance between the two tethering points was 5  $\text{\AA}$ .

**Explicit solvent simulations.** Pulling simulations of WT SOD1 were also performed in explicit water. Equilibrated starting structures were generated by placing the protein in a cubic box of simple point charge (SPC) water, such that all protein atoms were initially at least 20  $\text{\AA}$  from any cubic face. This required 10866 water molecules to solvate the protein. Prior to simulation, the energy of the system was minimized using a steepest descent algorithm. The system was then equilibrated for 20 ns under a constant volume (NVT) ensemble, with temperature maintained at 300 K using the Berendsen weak coupling method. Pulling simulations were then carried out using an integration time-step of 2 fs, and coordinates were saved every 100 ps. The long-distance cut-off used for non-bonded electrostatic and VDW interactions was 14  $\text{\AA}$ .

We have also minimized and equilibrated E,E (SS) WT, E,E (SH) WT and E,E G127X variants of SOD1 in explicit solvent following the same procedure as described above for Cu,Zn (SS) WT SOD1. Each of the variants was equilibrated for 35 ns, and the last 20 ns of that trajectory was used for the calculation of RMSF and backbone amide SASA.

**Tethering residues.** The  $C_\alpha$  atom of the residues listed in Table S2 were closest to the center of mass of the corresponding protein variant, and so were used as the central tether. Whenever the pulling residue appeared to be very close to the center of mass tethering residue, the tethering residue was shifted to the midpoint of the protein sequence to avoid artificially large forces. Specifically, for several variants listed in Table S2, residues 40, 45, 46, 50, 54 and 55 were either too close to the central  $C_\alpha$ , or were along the same beta strand as the central  $C_\alpha$ , and thus gave anomalous force-extension profiles probing covalent bonding topology more so than non-covalent stabilizing interactions. Thus when residues 40, 45, 46, 50, 54 and 55 were pulled, the tethering residue was moved to corresponding residue indicated in Table S2. This always resolved the problem of large forces, except for 1-110 SOD1. For this variant, we have taken residue 86, which is also close to the center of mass, because the midpoint residue (56) did not resolve the problem of anomalously large forces.

**Residues used for mechanical scans of protein stability.** We have previously developed a model calculation of the free energy of unfolding specific regions of a protein using the so-called single-sequence approximation [1], in analogy to similar models used in protein folding [26,27,28,29,30]. In this formalism, the resulting free energy landscape is constructed as a function of the center residue of the contiguous strand taken to be disordered, and the sequence length of the disordered strand. In our unfolding model, we have treated electrostatic and van der Waals energies in the system at the level of the CHARMM22 energy function [31,32]. Protein entropy was calculated from simulations of the unfolded ensemble in explicit solvent. Regions of low thermodynamic stabil-

ity may be projected onto the native structure; these regions constitute candidate epitopes for unfolding-specific immunologic therapy, providing that the criteria of residue-specific immunogenicity and uniqueness of the epitope sequence in the proteome are established. Antibodies that bind to disease-specific protein epitopes corresponding to non-native conformations displayed by disordered protein sequences have been developed for superoxide dismutase 1 (SOD1) [33] and Prion protein [34]. The candidate epitopes as determined from free energy landscape analysis for WT SOD1 are given in the table in Figure S1.

Every 5th residue along the protein sequence, including the first and last residues, was taken as a tethering residue. As well, the central positions of the predicted epitopes and anti-epitopes were added to the data set.

The first anti-epitope contains 5 residues with residue 18 at its center, however the free energy landscape prediction gave a larger stability to candidate epitope 1 than epitope 2 [1], so we chose residue 17 instead as potentially more representative for the stiff sequence of residues. For all other epitopes or anti-epitopes, either the center residue was chosen as the tethering point if the strand contains an odd number of residues, or if the strand contained an even number of residues, the pulling residue was chosen randomly between the two center residues.

If the center of the epitope happened to coincide with a multiple of 5 already included in the scan (e.g. residue 10), then the next residue (residue 11 in this case) was also taken. Thus a set of 48 residues was used in the mechanical scans: (1, 5, 10, 11, 15, 17, 20, 24, 25, 30, 31, 35, 38, 40, 45, 46, 50, 54, 55, 60, 65, 70, 73, 75, 80, 85, 90, 91, 95, 100, 101, 105, 108, 110, 115, 120, 121, 125, 130, 135, 136, 140, 141, 145, 146, 150, 151, 153).

**Proteins considered.** Proteins whose mechanical profiles were calculated are given in Table S2 below, along with the corresponding PDB entries used to generate equilibrated structures for simulations.

**Modeling proteins with no PDB structure.** Some proteins studied here have no PDB structural coordinates available; see Table S2. For these proteins, a structure was built by modifying known PDB structures of similar proteins. For example, metal-depleted (E,E (SS)) WT SOD1 was created from E,E (SS) SOD1 structure (1RK7) by back-mutating Q133E, E50F and E51G using the PyMOL software package [35]. Metal-depleted, disulfide-reduced (E,E (SH) WT) SOD1 was created from both E,E (SS) SOD1 structure (1RK7) by reducing the disulphide linkage and mutating E50F, E51G, and Q133E, and also from Cu,Zn (SS) WT SOD1 (1HL5) by reducing the disulphide linkage and removing the metals. The E,E G127X mutant was created from Cu,Zn (SS) WT SOD1 by removing the metals and the last 20 residues, and then mutating the last 6 residues of the remaining sequence (KGGNEE) to correspond to the frame-shifted non-native C-terminal peptide sequence (GGQRWK) prior to the termination sequence. The Cu,Zn G127X mutant was prepared following the same way as done for E,E G127X - only the metals were kept intact. The full-length C57S/C146S mutants were prepared from Cu,Zn (SS) WT SOD1 by mutating both Cys-57 and Cys-146 to Serine (Cu,Zn C57S/C146S 1-153) and simultaneously removing the metals (E,E C57S/C146S 1-153). The truncated versions of these variants were made by following the same technique as described for full-length proteins - only residues 128-153 were deleted for the truncated ones. E,E (SH) SOD1 variants 1-140 and 1-110 were created from the full length E,E (SH) WT SOD1 by deleting the last 13 and 43 residues respectively.

As described in the Methods subsection on steered MD simulations, all modified structures were energy minimized and equilibrated for 20 ns by running an equilibrium simulation, before performing any pulling assays.

**Gō model energetics.** The SMOG Gō model recipe used here [9] takes heavy atoms within 2.5 Å, and applies native contacts to them with a Lennard-Jones 6-12 potential. The SMOG Gō model recipe also attributes energies to dihedral terms in the BB and SCs. The energy scale determining well-depths for these interactions is given through the relation:  $N_c \epsilon_c + N_{BB} \epsilon_{BB} + N_{SC} \epsilon_{SC} = N_A \cdot (1 \text{ kJ/mol})$ , where  $N_c$  is the number of non-local contacts and  $\epsilon_c$  is their corresponding well-depth, and the other numbers correspond to BB and SC dihedral numbers and energy scales respectively.  $N_A$  on the right hand side is the number of atoms. The overall energy scale of all interactions is thus given by 1kJ/mol times the number of atoms in the system.

**Umbrella Sampling and Weighted Histogram Analysis Method (WHAM).** Initial configurations were obtained from pulling simulations as described in the Methods subsection on steered MD, to obtain 25 initial conditions between 0 and 5Å. These initial configurations are then simulated for 10ns each, in an umbrella potential with stiffness 500kJ/mol/nm<sup>2</sup> to constrain the simulations near their corresponding separation distances. The 25 simulations are then used to reconstruct the free energy profile along the distance coordinate using the weighted histogram analysis method (WHAM) [36], and the free energy difference between 0 and 5Å is then obtained.

**Metal insertion or extraction in calculating interaction energies.** To obtain free energies of metal binding, metals were inserted into or extracted from the putative binding locations for WT SOD1, and all glycine mutants of SOD1. Metals were always found to be at least metastable in their putative binding positions. To obtain the metal binding free energy, the most direct straight-line path was first determined for the pulling direction, by finding the approximate direction of highest solvent exposure of the metal. Tethers were placed on the metal, and on the closest  $C_\alpha$  atom opposite to the direction of highest solvent exposure. For Cu extraction this corresponded to tethering the  $C_\alpha$  atom of residue Phe45, and for Zn removal the corresponding  $C_\alpha$  atom tether was in Asp83.

The metal was pulled away from the protein using a spring constant of 500 kJ/mol/nm<sup>2</sup> and a pull rate of 0.01 nm/ps. For purposes of the free energy calculation, the final extension from the equilibrium distance between metal and tethering residue was taken to be approximately 30Å. From these trajectories, snapshots were taken to generate the starting configurations for the umbrella sampling windows [37,38,39]. An asymmetric distribution of sampling windows was used, such that the window spacing was 1Å between 0 and 20 Å separation, and 2Å beyond 20Å of separation. Such spacing allowed for increasing detail at smaller separation distances, and resulted in a total of 25 windows. In each window, 10 ns of MD was performed for a total simulation time of 250 ns utilized for umbrella sampling. Analysis of the results was performed using the weighted histogram analysis method (WHAM) [36].

To remove conformational distortion effects on the free energy, position restraints were applied to the protein in the following way. For a given  $C_\alpha$  atom in the protein, all other  $C_\alpha$  atoms within 5Å were constrained to have a roughly constant  $C_\alpha$ - $C_\alpha$  distance, the same as in an equilibrated structure, using spring constants of  $392 \times 10^3$  kJ/mol/nm<sup>2</sup>. Using  $C_\alpha$  constraints allows the protein to retain its structure un-

der force, while still allowing the side chains and partially the backbone to fluctuate in response to the external perturbation. After metal extraction,  $C_\alpha$  constraints were relaxed and the relaxation free energy was calculated as described below.

The free energy for metal extraction was corrected to account for protein relaxation in the final metal depleted state:  $\Delta F_{tot} = \Delta F_{constrained}^{extraction} + \Delta F_{relax}$ . That is, after metal extraction,  $C_\alpha$  constraints are gradually reduced from  $392 \times 10^3$  kJ/mol/nm<sup>2</sup> to zero using 30 windows and 10ns of relaxation time in each window, and the free energy change for this process is again obtained using WHAM. Convergence of the free energy values was tested by both varying the number of windows (to 30, 35 and 45) and varying the length of the equilibrium simulation in each window (to 15, 20, 25 and 30 ns). In all cases the free energies were seen to have converged using the original protocol.

To validate that equilibrium free energies have been obtained by this procedure, thermodynamic cycles were constructed by re-inserting the metal and equilibrating, for WT SOD1, and ALS-associated mutants A4V and G93A, as well as PTM variants Cu,E(SS) and E,Zn(SS) [11]. The metal binding free energies subject to  $C_\alpha$  constraints were calculated, as well as the subsequent relaxation free energies. The total free energy change over such cycles was typically less than 0.04 kJ/mol, confirming that the cycles are thermodynamic to within the error of the simulation. A more detailed description of the procedure is given in reference [11].

**Potential energy calculations.** Cu,Zn(SS) and E,E(SS) WT SOD1 protein structures were simulated in a cubic box with periodic boundary conditions and size such that all protein atoms were initially at least 20 Å from any cubic face. An all-atom representation of the protein was used, with OPLS-AA/L parameters [17,18], and a generalized Born surface area (GBSA) implicit solvent model [20] was used, with dielectric constants of the protein and solvent taken to be 4 and 80 respectively. The Onufriev-Bashford-Case (OBC) algorithm was used to calculate Born radii [19]. The phenomenological surface tension coefficient used in calculating solvation free energies was 0.005 kcal/mol/(Å<sup>2</sup>) [20]. The LINCS algorithm was applied to constrain all bond lengths that contained a hydrogen atom [21]. Prior to simulation, energy was minimized using a steepest descent algorithm to remove any potential steric clashes. Simulations were carried out with an integration time-step of 2 fs and coordinates were saved after every 100 ps. The long-distance cut-off used for non-bonded interactions was 14 Å for both Electrostatic and van der Waals (VDW) interactions.

For both the Cu,Zn(SS) and E,E(SS) WT SOD1 variants of SOD1 protein, a simulation was run for 20 ns to equilibrate the protein. Once equilibrium is reached, the potential energy was recorded and averaged over 50 snapshots, where each snapshot is taken every 0.5ns. The final equilibrated conformation was then mutated in PyMol to either one of the ALS-associated mutants described in the main text or alanine mutants described above. The mutated structures were then again equilibrated until convergence of the potential energy (typically  $\approx$  35ns). Then 50 snapshots were taken, once every 0.5ns, and these snapshots were used to obtain the ensemble-averaged potential energy of the mutant. In this way,  $\Delta \bar{U}_{WT \rightarrow MUT}$  is obtained for each mutant. A histogram of this quantity is plotted for the 30 non-ALS alanine mutants described in the above text, in Figure S18B.

**Frustratometer analysis.** Highly frustrated contacts were found using the “frustratometer” method of Ferreiro *et. al.*, given in reference [12]. This method finds the particular

contacts that are highly frustrated in a one protein conformation. Metal-protein interactions are not included in the frustratometer analysis; only protein-protein interactions are considered. We have used equilibrium protein conformations of the Cu,Zn(SS) and E,E(SS) states of SOD1 to distinguish the effect of metals on SOD1 protein structure. An equilibrium ensemble of 50 conformations was obtained for both WT SOD1 and mutants of SOD1, as described in the previous section above. The number of highly frustrated contacts within a sphere of 5Å around each  $C_\alpha$  atom was found for every snapshot, and averaged over snapshots. This number was again averaged over mutants to obtain the mutant and equilibrium ensemble-averaged number of highly frustrated contacts around a given  $C_\alpha$  atom.

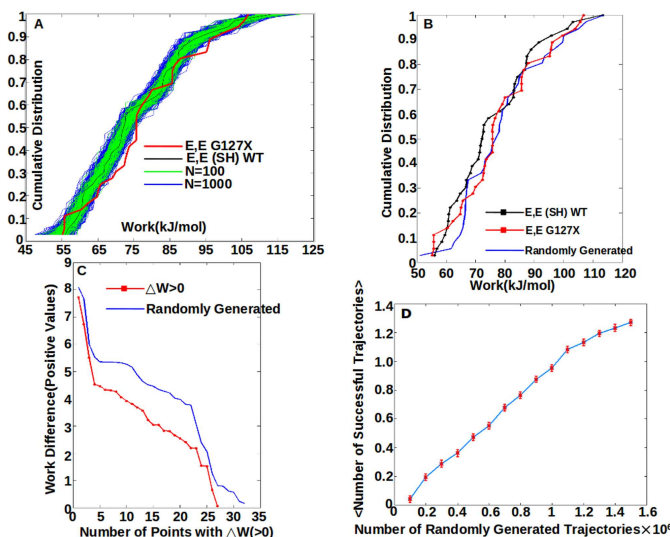


**Fig. S21.** A Statistical significance test between E,E (SH) WT SOD1 and E,E G127X cumulative distributions. The black curve denotes the E,E (SH) WT profile, and the red curve denotes the E,E G127X profile. The collection of green lines corresponds to 100 randomly-generated cumulative distributions in the following way: starting from the E,E (SH) WT work values, gaussian noise with zero mean and standard deviation  $\sigma = 2.7$  kJ/mol is added to each work value. The resulting collection of work values are then rank-ordered to generate a cumulative distribution, and this process is then repeated  $N$  times. The collection of blue lines corresponds to  $N = 1000$ . For large enough  $N$ , one will begin to find outlying cumulative distributions which deviate as much or more than a given trial distribution, here E,E G127X. An example of such an outlier is shown in panel B. In this case, the number of positive deviations (differences in work value) between the red and black curves in panel A are recorded (27), along with their work values, which are themselves rank ordered largest to smallest and plotted in panel C. An outlier at least as extreme as E,E G127X must have a set of positive work deviations such that the corresponding curve lies above the red curve in panel C. In this case the randomly generated outlier has 32 positive deviations in work, 27 of which are larger than those between E,E G127X and E,E (SH) WT variants. The number of randomly generated trajectories is increased, until the mean number of successful trajectories, corresponding to the criterion in panel C, exceeds unity. A plot of the mean number of successful trajectories as a function of  $N$  is given in panel D. The statistical significance  $p$  of a given trajectory is then given as  $p = 1/N_1$ , where  $N_1$  is the number of randomly generated trajectories that give an expectation value of unity for the number of successfully-generated outliers. In this case, the statistical significance of E,E G127X is about  $1/(1.1 \times 10^6)$ , or about  $9 \times 10^{-7}$ .

**Statistical Analysis.** The mechanical profile is a collection of 48 work values for a given SOD1 variant. Each work value measured from our simulations is accurate to some  $\sigma$  kJ/mol which we determine as follows. The difference in the mechanical scans of two initial conditions, for example as derived

from different crystal structures, gives a measure of the error in the mechanical scan. For E,E (SH) WT SOD1 shown in the main panel of Figure S4, the work difference  $\Delta W$  has mean 0.03kJ/mol and standard deviation  $\sigma_o = 2.1$ kJ/mol. A  $z$ -test indicates that with 93% certainty the values of  $\Delta W$  arise from a gaussian distribution of mean zero and variance  $\sigma_o$ . On the other hand, the values of  $\Delta W$  in the inset A of Figure S4 for Cu,Zn (SS) WT SOD1 have mean 0.75kJ/mol and standard deviation 1.5kJ/mol. This distribution fails a  $z$ -test for a gaussian with mean zero and  $\sigma_o = 1.5$ kJ/mol, indicating that the error in measurement is larger than  $\sigma_o$ . We increase the standard deviation until the  $z$ -test indicates the data arises from a gaussian of mean zero and standard deviation  $\sigma$ . This gives  $\sigma = 2.7$ kJ/mol, which we use as a measure of the error bars in the work values of the mechanical profile.

In comparing two mechanical profiles residue by residue, the probability of finding the second profile by chance, given the measurements  $W_i$  of the first profile, and the error bars  $\sigma$ , is:

$$P(\{\Delta W_i\}) = \frac{1}{2} \prod_{i=1}^N \operatorname{erfc} \left( \frac{|\Delta W_i|}{\sqrt{2}\sigma} \right). \quad [1]$$

where  $|\Delta W_i|$  is the modulus of the difference between the two work values for residue  $i$ , and  $N = 48$  here.

Comparing two cumulative distributions is more forgiving, in that there is a greater likelihood two different mechanical profiles may still give the same overall work distribution. These two protein variants might then be said to have the same overall mechanical stability, although what parts of the structure were the most or least stable would differ for each protein.

Because the overall variance of a given work profile is so large however (typically  $\approx 15$  kJ/mol), it is very likely to obtain the cumulative distribution of any one variant from any other variant by a direct Kolmogorov-Smirnov test. We are interested in a different question however: given one work profile, its cumulative distribution, and the error bars associated with the work values, what is the probability of obtaining a cumulative distribution at least as extreme as another given one by chance, i.e. as arising from the original work profile? This is a complicated question because it is non-trivial to account for the combinatorial number of ways of obtaining a given cumulative distribution.

To find the above probability, and thus determine the statistical significance of a given cumulative distribution, we employ a ‘‘Monte Carlo’’ procedure of generating cumulative distributions from a given ‘‘baseline’’ work profile. For example, to test the effect of truncation at the C-terminus which mechanically stabilizes the protein, we wish to find the probability of obtaining the E,E G127X cumulative distribution (or a distribution even more stabilized) from the E,E (SH) WT SOD1 cumulative distribution. The E,E G127X cumulative distribution has 30 work values that are more stable than those in the E,E (SH) WT SOD1 cumulative distribution; the difference in work values are plotted in Figure S21 panel C, largest to smallest. We seek cumulative distributions that have rank ordered deviations at least as large as those of the E,E G127X cumulative distribution.

Work profiles are constructed by adding gaussian noise to a the baseline work profile (here that of E,E (SH) WT SOD1), where the gaussian noise has mean zero and standard deviation  $\sigma = 2.7$  kJ/mol. A cumulative distribution is then constructed for each generated profile by sorting the values lowest to highest. After constructing  $N$  of such cumulative distributions, we ask whether one has found a cumulative distribution with, e.g. rank-ordered positive deviations at least as large as those in the E,E G127X cumulative distribution.

The value of  $N$  where the expected number of trajectories is unity determines the statistical significance:  $p = 1/N$ . Plots of the corresponding distributions for E,E (SH) WT SOD1 and E,E G127X SOD1 are given in Figure S21.

If 2 cumulative distributions are different, their mechanical fingerprints are necessarily different. If they are the same,

their fingerprints can always be compared to discern the effects of mutation. In practice however we never encountered two different fingerprints that gave rise to indistinguishable cumulative distributions.

- Cashman, N. R., Plotkin, S. S., & Guest, W. C. (2010) Us patent 12/574,637: Methods and systems for predicting misfolded protein epitopes; 9/16/10.
- Colizzi, F., Perozzo, R., Scapozza, L., Recanatini, M., & Cavalli, A. (2010) Single-molecule pulling simulations can discern active from inactive enzyme inhibitors. *J. Am. Chem. Soc.* 132, 7361–7371.
- Lu, H., Israelewitz, B., Krammer, A., Vogel, V., & Schulten, K. (1998) Unfolding of titin immunoglobulin domains by steered molecular dynamics simulation. *Biophys. J.* 75, 662–671.
- Lu, H. & Schulten, K. (1999) Steered molecular dynamics simulations of force-induced protein domain unfolding. *Proteins: Struct. Funct. Bioinfo.* 35, 453–463.
- Strange, R. W., et al. (2003) The Structure of Holo and Metal-deficient Wild-type Human Cu, Zn Superoxide Dismutase and its Relevance to Familial Amyotrophic Lateral Sclerosis. *J. Mol. Biol.* 328, 877–891.
- Strange, R. W., et al. (2006) Variable metallation of human superoxide dismutase: Atomic resolution crystal structures of Cu–Zn, Zn–Zn and As-isolated wild-type enzymes. *J. Mol. Biol.* 356, 1152–1162.
- Banci, L., Bertini, I., Cramaro, F., Del Conte, R., & Viezzoli, M. S. (2003) Solution Structure of Apo Cu,Zn Superoxide Dismutase: Role of Metal Ions in Protein Folding. *Biochemistry* 42, 9543–9553.
- Gō, N. & Taketomi, H. (1978) Respective roles of short- and long-range interactions in protein folding. *Proc. Natl. Acad. Sci. USA* 75, 559–563.
- Whitford, P. C., et al. (2009) An all-atom structure-based potential for proteins: Bridging minimal models with all-atom empirical forcefields. *Proteins: Struct. Funct. Bioinfo.* 75, 430–441.
- Lindberg, M. J., Bystrom, R., Boknas, N., Andersen, P. M., & Oliveberg, M. (2005) Systematically perturbed folding patterns of amyotrophic lateral sclerosis (als)-associated sod1 mutants. *Proc. Natl. Acad. Sci. USA* 102, 9754–9759.
- Das, A. & Plotkin, S. S. (2012) Mechanical probes of SOD1 predict systematic trends in metal and dimer affinity of ALS-associated mutants. *J. Mol. Biol.* "(In Press)".
- Ferreiro, D. U., Hegler, J. A., Komives, E. A., & Wolynes, P. G. (2011) On the role of frustration in the energy landscapes of allosteric proteins. *Proc. Natl. Acad. Sci. USA* 108, 3499–3503.
- Sotomayor, M. & Schulten, K. (2007) Single-molecule experiments in vitro and in silico. *Science* 316, 1144–1148.
- Carrion-Vazquez, M., et al. (2003) The mechanical stability of ubiquitin is linkage dependent. *Nat. Struct. Biol.* 10, 738–743.
- Irbäck, A., Mitternacht, S., & Mohanty, S. (2005) Dissecting the mechanical unfolding of ubiquitin. *Proc. Natl. Acad. Sci. USA* 102, 13427–13432.
- Imparato, A. & Pelizzola, A. (2008) Mechanical unfolding and refolding pathways of ubiquitin. *Phys. Rev. Lett.* 100, 158104–1–158104–4.
- Jorgensen, W., Maxwell, D., & Tirado-Rives, J. (1996) Development and testing of the OPLS all-atom force field on conformational energetics and properties of organic liquids. *J. Am. Chem. Soc.* 118, 11225–11236.
- Kaminski, G. A. & Friesner, R. A. (2001) Evaluation and reparametrization of the OPLS-AA force field for proteins via comparison with accurate quantum chemical calculations with peptides. *J. Phys. Chem. B* 105, 6474–6487.
- Onufriev, A., Bashford, D., & Case, D. (2004) Exploring protein native states and large-scale conformational changes with a modified Generalized Born model. *Proteins: Struct. Funct. Genet.* 55, 383–394.
- Bjelkmar, P., Larsson, P., Cuendet, M. A., Hess, B., & Lindahl, E. (2010) Implementation of the CHARMM force field in GROMACS: analysis of protein stability effects from correlation maps, virtual interaction sites, and water models. *J. Chem. Theo. Comp.* 6, 459–466.
- Hess, B., Bekker, H., Berendsen, H. J. C., & Fraaije, J. G. E. M. (1997) LINCS: a linear constraint solver for molecular simulations. *J. Comp. Chem.* 18, 1463–1472.
- Lv, S., et al. (2010) Designed biomaterials to mimic the mechanical properties of muscles. *Nature* 465, 69–73.
- Lemkul, J. A. & Bevan, D. R. (2010) Assessing the stability of alzheimer's amyloid protofibrils using molecular dynamics. *J. Phys. Chem. B* 114, 1652–1660.
- Kim, T., Rhee, A., & Yip, C. M. (2006) Force-induced insulin dimer dissociation: A molecular dynamics study. *J. Am. Chem. Soc.* 128, 5330–5331.
- Gerini, M. F., Roccatano, D., Baciocchi, E., & Nola, A. D. (2003) Molecular dynamics simulations of lignin peroxidase in solution. *Biophys. J.* 84, 3883–3893.
- Plotkin, S. S., Wang, J., & Wolynes, P. G. (1996) Correlated energy landscape model for finite, random heteropolymers. *Phys. Rev. E* 53, 6271–6296.
- Hiiser, V. J. & Freire, E. (1996) Structure-based calculation of the equilibrium folding pathway of proteins. correlation with hydrogen exchange protection factors. *J. Mol. Biol.* 262, 756–772.
- V. Muñoz and W. A. Eaton. (1999) A simple model for calculating the kinetics of protein folding from three-dimensional structures. *Proc. Natl. Acad. Sci. USA* 96, 11311–11316.
- Alm, E. & Baker, D. (1999) Prediction of protein-folding mechanisms from free-energy landscapes derived from native structures. *Proc. Natl. Acad. Sci. USA* 96, 11299–11310.
- Galzitskaya, O. V. & Finkelstein, A. V. (1999) A theoretical search for folding/unfolding nuclei in three dimensional protein structures. *Proc. Natl. Acad. Sci. USA* 96, 11299–11304.
- Guest, W., Cashman, N. R., & Plotkin, S. S. (2010) Electrostatics in the stability and misfolding of the prion protein: Salt bridges, self-energy, and solvation. *Biochem. Cell Biol.* 88, 371–381.
- Guest, W. C., Cashman, N. R., & Plotkin, S. S. (2011) A theory for the anisotropic and inhomogeneous dielectric properties of proteins. *Phys. Chem. Chem. Phys.* 13, 6286–6295.
- Rakhit, R., et al. (2007) An immunological epitope selective for pathological monomer-misfolded SOD1 in ALS. *Nat. Med.* 13, 754–759.
- Paramithiotis, E., et al. (2003) A prion protein epitope selective for the pathologically misfolded conformation. *Nat. Med.* 9, 893–899.
- DeLano, W.L. (2002) The PyMOL molecular graphics system. <http://www.pymol.org>.
- Kumar, S., Rosenberg, J. N., Bouzida, D., Swendsen, R. H., & Kollman, P. A. (1992) The weighted histogram analysis method for free-energy calculations on biomolecules. I. The method. *J. Comput. Chem.* 13, 1011–1021.
- Patey, G. N. & Valleau, J. P. (1973) The free energy of spheres with dipoles: Monte carlo with multistage sampling. *Chem. Phys. Lett.* 21, 297–300.
- Torrie, G. M. & Valleau, J. P. (1974) Monte Carlo free energy estimates using non-Boltzmann sampling: Application to the sub-critical Lennard-Jones fluid. *Chem. Phys. Lett.* 28, 578–581.
- Torrie, G. M. & Valleau, J. P. (1977) Nonphysical sampling distributions in monte carlo free-energy estimation: Umbrella sampling. *J. Comput. Phys.* 23, 187–199.

## Supporting Information Tables

**Table S1. Correlation table of Work(upper diagonal) and RMSF(lower diagonal) values for different variants of SOD1**

RMSF/Work	Cu,Zn (SS) WT	E,E (SS) WT	E,E (SH) WT	E,E G127X	E,E 1-140	E,E 1-110
Cu,Zn (SS) WT	1/1	-0.37	-0.16	0.20	0.06	0.14
E,E (SS) WT	0.16	1/1	0.51	-0.17	-0.03	0.22
E,E (SH) WT	0.10	0.51	1/1	-0.09	-0.13	0.38
E,E G127X	0.06	-0.14	0.13	1/1	0.32	0.62
E,E 1-140	0.02	0.09	0.11	0.21	1/1	0.56
E,E 1-110	0.03	0.13	0.11	0.21	0.22	1/1

Correlations are generally insignificant. The two significant correlations are between E,E G127X and E,E 1-110 ( $p=1.0e-4$ ), and E,E 1-140 and E,E 1-110 ( $p=6.2e-4$ ).

**Table S2. Central tethering residues for mechanical profiles**

SOD1 variant	Tethering residue	PDB ID used for structure generation
Cu,Zn (SS) WT	46 (76 <sup>‡</sup> )	1HL5, 2C9V
E,E (SS) WT	46 (76 <sup>‡</sup> )	1RK7 <sup>†</sup>
E,E (SH) WT	46 (76 <sup>‡</sup> )	1HL5, 1RK7 <sup>†</sup>
Cu,Zn G127X	45 (67 <sup>‡</sup> )	1HL5*
E,E G127X	45 (67 <sup>‡</sup> )	1HL5*
E,E 1-140	46 (71 <sup>‡</sup> )	1HL5
E,E 1-110	46 (86 <sup>‡</sup> )	1HL5
Cu,Zn C57S/C146S 1-153	46 (76 <sup>‡</sup> )	1HL5 <sup>⊕</sup>
E,E C57S/C146S 1-153	46 (76 <sup>‡</sup> )	1HL5 <sup>⊕</sup>
Cu,Zn C57S 1-127	45 (64 <sup>‡</sup> )	1HL5 <sup>⊖</sup>
E,E C57S 1-127	45 (64 <sup>‡</sup> )	1HL5 <sup>⊖</sup>

<sup>‡</sup>for residue 40, 45, 46, 50, 54 and 55.

<sup>†</sup>Structures reported have mutations from the WT sequence; these were “back-mutated” to construct structures for the WT sequence, as described in the Methods subsection on modeling proteins with no PDB structure.

\*residues 134-153 deleted and 128-133 mutated.

<sup>⊕</sup>Cys-57 and Cys-146 mutated to Serine.

<sup>⊖</sup>Cys-57 mutated to Serine and residues 128-153 deleted.

**Table S3. Proteins considered for Frustratometer results and Interaction Energy calculations**

Frustratometer	Interaction Energy
A4V,G37R,L38V,G41D,G41S,H43R, H46R,H46R/H48Q,T54R,D76Y,H80R, L84F,G85R,D90A,G93A,G93C,E100G, I113T,D124V,D125H,S134N,L144F <sup>‡</sup>	A4G,L8G,I17G,L38G,H43G,H46G, H46G/H48G,T54G,D76G,H80G,D83G,L84G, D90G,E100G,I113G,R115G,D124G,D125G, S134G,A140G,R143G,L144G,V148G,I149G <sup>†</sup>
V5A,G10A,Q15A,F20A,S25A, K30A,I35A,E40A,F45A,F50A, G56A,S59A,N65A,K70A,K75A, H80A,G85A,K91A,D96A,E100A, A105A,H110A,R115A,H120A,D125A, G130A,T135A,N139A,L144A,G150A*	A1G,P13G,E21G,Q22G,K23G,E24G,S25G,N26G,P28G,V31G,S34G, E40G,E49G,F50G,D52G,N53G,A55G,C57G,T58G,S59G,A60G,P62G, H63G,F64G,N65G,P66G,L67G,S68G,R69G,K70G,H71G,P74G,K75G, E77G,E78G,R79G,V81G,N86G,A89G,V94G,A95G,D101G,S102G,V103G, I104G,S105G,L106G,S107G,D109G,H110G,C111G,I112G,H120G,E121G,K122G, A123G,L126G,K128G,N131G,E132G,E133G,T135G,K136G,T137G,N139G,S142G <sup>⊕</sup>

<sup>‡</sup>Proteins used for Figure 3.

<sup>†</sup>Proteins used for Figure 5, Figure S18 and Figure S19.

\*Proteins used for Figure S18.

<sup>⊕</sup>Proteins used for Figure S18 and Figure S19.

**Table S4.** Mechanical work values of WT SOD1 variants - the values reported in the table depict the work in kJ/mol needed to pull a particular residue up to 5 Å. †

Residue Index	Cu,Zn (SS) WT	E,E (SS) WT	E,E (SH) WT	Cu,Zn G127X	E,E G127X	Cu,Zn 1-153 C57S/C146S	E,E 1-153 C57S/C146S	Cu,Zn 1-127 C57S	E,E 1-127 C57S	E,E 1-140	E,E 1-110
1	66.32	63.90	60.32	62.47	60.37	67.12	61.25	64.62	66.37	61.09	54.08
5	68.85	74.92	88.95	71.83	75.80	76.02	81.27	70.66	72.22	66.40	68.90
10	66.18	94.68	81.29	82.38	86.41	92.94	72.22	75.83	61.27	70.19	72.00
11	108.41	62.53	59.51	68.39	65.69	70.20	66.80	64.41	80.27	64.09	58.71
15	89.97	71.56	68.81	99.48	104.00	77.44	91.12	75.83	69.37	88.09	76.67
17	91.53	61.60	45.15	99.48	95.69	73.91	66.87	72.83	72.27	94.09	67.84
20	78.24	67.77	60.67	67.49	64.74	87.41	82.12	76.87	90.29	92.40	65.87
24	58.82	54.46	56.77	57.99	55.69	67.01	72.22	69.32	81.29	64.09	52.77
25	62.31	126.04	87.35	70.39	72.65	73.22	78.18	65.93	77.22	74.69	69.98
30	42.90	124.00	113.40	51.00	54.39	76.48	59.16	84.37	68.22	73.50	72.93
31	66.38	76.52	55.92	81.20	85.69	67.20	71.29	65.02	69.22	74.09	65.59
35	77.33	104.09	84.16	79.39	76.61	66.55	69.27	76.93	72.12	62.59	67.33
38	67.11	63.59	64.74	79.43	75.69	76.01	80.18	70.77	78.20	54.09	57.77
40	94.41	98.00	91.57	75.48	73.67	68.33	90.19	87.83	71.22	59.20	64.95
45	83.49	64.31	68.18	67.88	65.04	76.04	81.20	64.83	61.22	76.90	61.17
46	63.32	56.23	66.83	79.97	75.69	66.12	71.27	74.44	60.27	84.09	67.54
50	57.08	112.86	78.24	71.98	73.14	73.51	69.37	70.73	59.38	67.59	63.63
54	85.03	51.12	71.63	59.99	55.69	60.20	61.11	60.84	67.37	64.09	59.27
55	88.66	78.95	72.65	94.99	95.16	69.05	58.27	59.86	78.22	80.09	76.12
60	79.50	79.77	58.41	65.00	69.98	75.93	66.27	65.37	81.29	91.19	66.11
65	92.99	76.29	83.28	88.99	87.99	86.94	71.27	66.83	61.29	66.19	72.21
70	80.56	64.42	95.86	68.34	69.06	66.07	58.33	77.79	58.48	94.30	73.95
73	125.06	43.42	60.82	107.09	105.69	70.20	71.22	94.93	69.32	104.09	78.50
75	72.82	94.37	71.42	59.49	55.12	78.13	65.37	75.94	66.33	69.90	58.25
80	73.18	42.31	72.12	98.40	99.67	68.05	80.33	73.90	78.22	72.09	72.58
85	72.10	77.37	70.86	56.49	54.14	66.76	66.76	72.08	61.22	85.40	64.01
90	87.98	62.90	74.42	78.49	80.03	83.32	71.22	63.88	69.44	59.40	62.38
91	98.44	46.27	61.36	58.40	55.69	74.91	90.44	76.04	82.22	54.09	53.91
95	61.74	90.15	82.99	97.88	96.10	84.16	62.22	85.33	90.19	101.20	81.48
100	97.82	81.67	87.44	57.39	54.90	73.11	71.27	70.93	81.22	78.19	71.92
101	65.32	75.58	40.28	82.39	85.69	74.20	66.66	75.93	78.79	84.09	66.99
105	73.50	71.67	63.50	65.30	62.21	80.68	77.72	82.02	71.22	71.90	61.38
108	69.29	54.35	40.29	77.00	75.69	66.12	81.18	70.04	80.12	64.09	56.23
110	66.24	96.08	86.64	82.47	79.07	73.55	60.38	65.88	71.29	96.50	55.02
115	81.13	57.64	72.76	101.09	106.83	76.08	71.29	83.90	66.65	61.59	*
120	81.67	58.15	101.18	87.30	85.65	81.57	59.33	66.02	61.20	81.19	*
121	113.67	59.55	66.77	78.02	75.69	70.44	56.48	85.00	59.43	84.09	*
125	64.12	83.58	82.85	76.00	77.76	70.37	61.22	65.32	66.22	71.30	*
127	-	-	-	-	-	-	-	64.02	70.69	-	*
130	87.92	68.13	103.14	71.32	72.34	86.75	71.27	*	*	55.59	*
133	-	-	-	68.03	66.35	-	-	*	*	-	*
135	79.41	116.09	85.13	*	*	96.52	80.69	*	*	62.29	*
136	62.52	46.75	70.28	*	*	67.12	71.22	*	*	74.09	*
140	99.75	77.40	92.17	*	*	74.94	66.66	*	*	57.70	*
141	147.35	58.33	56.82	*	*	64.76	71.22	*	*	*	*
145	72.82	62.23	76.21	*	*	66.20	60.16	*	*	*	*
146	80.53	45.31	61.20	*	*	67.12	61.29	*	*	*	*
150	68.12	74.84	80.22	*	*	74.76	66.44	*	*	*	*
151	76.67	61.72	66.17	*	*	73.83	61.27	*	*	*	*
153	69.05	69.50	60.34	*	*	66.12	60.33	*	*	*	*

† “\*” indicates residues that are not present in the given variant, while “-” indicates work values that were not measured for a given variant.